

Downloaded from https://academic.oup.com/mnras/article/505/1/523/6271327 by University of Arizona Library user on 02 January 2024

Black hole magnetic fields and their imprint on circular polarization images

Angelo Ricarte, 1,2★ Richard Qiu^{3,4} and Ramesh Narayan^{1,2}

- ¹Center for Astrophysics | Harvard & Smithsonian, 60 Garden Street, Cambridge, MA 02138, USA
- ²Black Hole Initiative at Harvard University, 20 Garden Street, Cambridge, MA 02138, USA
- ³Department of Physics, Harvard University, 17 Oxford Street, Cambridge, MA 02138, USA

Accepted 2021 April 29. Received 2021 April 22; in original form 2021 March 1

ABSTRACT

The circular polarization of black hole accretion flows can encode properties of the underlying magnetic field structure. Using general relativistic magnetohydrodynamic (GRMHD) simulations, we study the imprint of magnetic field geometry on circular polarization images potentially observable by the *Event Horizon Telescope* (*EHT*). We decompose images into the different mechanisms that generate circular polarization in these models that are sensitive to both the line-of-sight direction and twist of the magnetic field. In these models, a stable sign of the circular polarization over time, as observed for several sources, can be attributed to a stability of these properties. We illustrate how different aspects of a generic helical magnetic field geometry become imprinted on a circular polarization image. We also identify novel effects of light bending that affect the circular polarization image on event horizon scales. One consequence is the sign flipping of successive photon rings in face-on systems, which if observable and uncorrupted by Faraday rotation, can directly encode the handedness of the approaching magnetic field.

Key words: accretion, accretion discs – black hole physics – magnetohydrodynamics (MHD) – polarization – techniques: polarimetric – galaxies: individual (M87).

1 INTRODUCTION

Supermassive black holes (SMBHs) are thought to reside at the centres of all massive galaxies, where they sometimes shine as active galactic nuclei (AGN) and help regulate star formation via AGN feedback (e.g. Kormendy & Ho 2013). Detailed studies of their central engines are important to better understand their accretion and feedback processes. By performing very long baseline interferometry at 1.3 mm, the *Event Horizon Telescope* (*EHT*) collaboration produced the first resolved images of the SMBH at the centre of M87, enabling novel studies of accretion physics on event horizon scales (Event Horizon Telescope Collaboration 2019a, b, c, d, e, f, 2021a, b).

The SMBH of M87, henceforth M87*, is believed to be fed by an advection dominated accretion flow of hot, tenuous plasma (Ichimaru 1977; Rees et al. 1982; Narayan & Yi 1994, 1995; Abramowicz et al. 1995; Reynolds et al. 1996a; Yuan & Narayan 2014). Its image is sensitive to properties intrinsic to the SMBH, including spin and accretion rate, as well as those of the plasma in the surrounding environment, such as the magnetic field configuration, temperature, and underlying electron distribution function. Combining multiwavelength constraints with the first resolved image of M87* enabled Event Horizon Telescope Collaboration (2019e) to narrow the allowed parameter space of M87*, ultimately ruling out all non-spinning SMBH models.

Recently, the EHT Collaboration completed an analysis of the linear polarization of M87*, providing novel insights into its magnetic field structure in particular (Event Horizon Telescope Collaboration

* E-mail: angelo.ricarte@cfa.harvard.edu

2021a, b; Goddi et al. 2021). Synchrotron emission, which dominates the millimetre image, is initially generated perpendicular to the local magnetic field, such that its polarization carries with it an imprint of the field geometry (Palumbo, Wong & Prather 2020). Then, as this polarization propagates, it is further modified by Faraday effects, important for depolarizing accretion flows down to observed levels and generating the observed rotation measure (Ballantyne, Özel & Psaltis 2007; Mościbrodzka et al. 2017; Jiménez-Rosales & Dexter 2018; Ricarte et al. 2020). Fully polarized radiative transport simulations on EHT scales have been developed in the past few decades, allowing us to link polarized images to the detailed physics of the underlying plasma and the space-time producing them (Bromley, Melia & Liu 2001; Broderick & Loeb 2006; Broderick & McKinney 2010; Porth et al. 2011; Shcherbakov, Penna & McKinney 2012; Dexter 2016; Mościbrodzka & Gammie 2018). This enabled (Event Horizon Telescope Collaboration 2021b) to discriminate between two major classes of accretion disc: a 'Magnetically Arrested Disk' (MAD) and 'Standard and Normal Evolution' (SANE). MAD accretion discs have magnetic fields strong enough to affect the disc dynamics and exhibit stronger poloidal (or non-toroidal) magnetic field components (Bisnovatyi-Kogan & Ruzmaikin 1974; Igumenshchev, Narayan & Abramowicz 2003; Narayan, Igumenshchev & Abramowicz 2003; Chael, Narayan & Johnson 2019). Meanwhile, the weaker magnetic fields of a SANE disc are sheared out by the motion of the plasma into a mostly toroidal configuration (Narayan et al. 2012; Sądowski et al. 2013; Ryan et al. 2018). The fractional linear polarization of M87*, the upper limit on its circular polarization, and most importantly the 'twisty pattern' of its spatially resolved linear polarization map favour 'MAD' models of M87* (Event Horizon Telescope Collaboration 2021b).

⁴ John A. Paulson School of Engineering and Applied Sciences, Harvard University, 29 Oxford Street, Cambridge, MA 02138, USA

524 A. Ricarte, R. Qiu and R. Narayan

In addition to these recent studies of M87*, there exist unresolved polarimetric measurements of Sgr A* and other low-luminosity AGN (Plambeck et al. 2014; Kim et al. 2019). In particular, linear polarization measurements of Sgr A* in the millimetre span two decades, motivating further studies of time variable polarimetry (Aitken et al. 2000; Bower et al. 2003; Marrone 2006; Muñoz et al. 2012; Bower et al. 2018). Moreover, although there is only an upper limit on the total circular polarization of M87* so far (≤0.8 per cent Goddi et al. 2021), the EHT Collaboration plans to one day produce images of circular polarization in addition to linear. Circularly polarized images of SMBH accretion flows are less well studied than their linearly polarized counterparts. For several observed sources, a persistent magnitude and sign of total circular polarization has been interpreted as stability in something inherent to the accretion flow such as its magnetic field geometry, but the details are poorly understood (Wardle & Homan 2001; Beckert & Falcke 2002; Ruszkowski & Begelman 2002; Enßlin 2003). One recent study of MAD accretion discs highlights the importance of both Faraday rotation and conversion and points out a sign inversion in the photon ring (Moscibrodzka, Janiuk & De Laurentis 2021).

There are two mechanisms that can generate circular polarization in these systems: intrinsic emission of circular polarization, and Faraday conversion of linear polarization (e.g. Wardle & Homan 2003). Synchrotron emission is the dominant emission mechanism in the millimetre, and it has an intrinsic linear polarization fraction of about 70 per cent (e.g. Pandya et al. 2016). In contrast, its emitted circular polarization fraction is only around 1 per cent, but this may be significant enough to contribute to the modest circular polarization fractions that have been measured for low-luminosity AGN. The sign of intrinsically emitted circular polarization directly encodes the direction of the magnetic field with respect to the photon wavevector. Meanwhile, Faraday conversion exchanges linear and circular polarization, with an efficiency depending on the temperature, density, and magnetic field of the plasma through which the light is travelling (e.g. Kennett & Melrose 1998). While the intensity of intrinsic emission increases with temperature, Faraday conversion is more efficient at lower (sub-relativistic) temperatures (Jones & Odell 1977). Both the intrinsic circular polarization fraction and the strength of Faraday conversion are sensitive to the composition of the underlying plasma. This allows circular polarization measurements to provide some of the most direct constraints on plasma composition (Wardle et al. 1998; Anantua et al. 2020; Emami et al. 2021).

Interestingly, Faraday conversion has no effect in a plasma with a uni-directional magnetic field without an additional mechanism to rotate the polarization plane. A synergy between Faraday conversion and Faraday rotation is one mechanism to accomplish this, as discussed in depth with general relativistic magnetohydrodynamic (GRMHD) models in Tsunetoe et al. (2020a, b). Alternatively, a line-of-sight twist in the magnetic field can also effectively rotate the polarization, by instead rotating the basis in which the polarization states are defined (Hodge 1982; Wardle & Homan 2001). This phenomenon is believed to set the circular polarization of jets on larger scales (e.g. Gabuzda et al. 2008). As we shall show, a more complicated magnetic field structure, combined with light bending effects, produces a rich circular polarization image on event horizon scales.

In this work, we study in detail the mechanisms that generate circular polarization in SMBH accretion flows using two GRMHD simulations, described in Section 2. To better understand the connection between circular polarization and magnetic field, we first study the structure of the magnetic field in these models in Section 3. Then, in Section 4, we study each of the mechanisms for generating circular

polarization in turn. We discuss the more general implications of this study in Section 5, and summarize our results in Section 6.

2 METHODOLOGY

We use as our starting point two GRMHD simulations of M87* that are included in Event Horizon Telescope Collaboration (2019e), Event Horizon Telescope Collaboration (2021b), one MAD and one SANE, both run using HARM (Gammie, McKinney & Tóth 2003). Although a SANE model is disfavoured for M87* based on linear polarization (Event Horizon Telescope Collaboration 2021b), it remains instructive to explore how such a system differs in its circularly polarized image. Both models have dimensionless spin parameter $a_{\bullet} = 0.94$ and are run using a variation of Kerr-Schild coordinates ('Funky Modified Kerr-Schild') that concentrates resolution at the mid-plane. These simulations are seeded with a weak dipolar magnetic field parallel to both the spin of the black hole (BH) and the angular momentum of the accretion disc. The MAD simulation is performed using a $384 \times 192 \times 192$ grid with a maximum radius of 10^3 GM_• c^{-2} , while the SANE simulation uses a 288 \times 128 \times 128 grid and a maximum radius of 50 $GM_{\bullet}c^{-2}$. (Throughout this work, G is the gravitational constant, M_{\bullet} is the SMBH mass, and c is the speed of light.) As in Ricarte et al. (2020), we only evolve the radiative transfer equations within a radius of $20 GM_{\bullet} c^{-2}$, inside of which we find the simulations exhibit inflow equilibrium. In Appendix B, we demonstrate that this region encloses the relevant plasma for producing circular polarization in these models. Both models are evolved to $10^4 GM_{\bullet} c^{-3}$, and we focus our presentation on the images of their final snapshots.

To perform the General Relativistic Ray Tracing (GRRT), we use IPOLE, a ray-tracing code that first solves the null geodesic equation from the camera through the source, then integrates forward the fully polarized radiative transfer equation (Mościbrodzka & Gammie 2018). Unless otherwise noted, images are created at a frequency of 228 GHz, with a field of view of $160~\mu$ as, and an angular resolution of $0.5~\mu$ as. As in many previous works, the plasma is modelled as two-temperature, where the ratio of the ion temperature to the electron temperature is a function of the plasma β parameter $\beta = p_{\rm gas}/p_{\rm mag}$ via

$$\frac{T_i}{T_e} = R_{\text{high}} \frac{\beta^2}{1 + \beta^2} + \frac{1}{1 + \beta^2},\tag{1}$$

where $p_{\rm gas}$ and $p_{\rm mag}$ are the gas and electron pressures respectively (Mościbrodzka, Falcke & Shiokawa 2016). As a consequence, $T_i = T_e$ in the highly magnetized funnel region, while $T_i/T_e \to R_{\rm high}$ in the gas pressure supported mid-plane. For details of the radiative transfer coefficients, we refer readers to Mościbrodzka & Gammie (2018), and the modification to the Faraday rotation coefficient ρ_V in Ricarte et al. (2020).

In the two models considered in this work, we fix $R_{\rm high} = 20$, a modest value motivated by recent studies of plasma heating (Mizuno et al. in preparation). For images with $R_{\rm high} = 160$, we comment that the signals we discuss in the paper remain largely unchanged, but there is additional 'noise' and depolarization due to the increased Faraday rotation. This is because larger values of $R_{\rm high}$ decrease the electron temperature in the gas pressure supported mid-plane, by construction, making Faraday effects more efficient. Meanwhile, for $R_{\rm high} = 1$, the MAD image is largely unchanged, but the SANE image exhibits a stronger photon ring feature discussed in Section 4.3.2, which is suppressed for $R_{\rm high} = 20$ due to Faraday rotation.

Since GRMHD simulations are scale free, the SMBH mass, distance, and accretion rate are set during the GRRT step. To set the spatial and temporal scales, we adopt a mass of $6.2 \times 10^9 \ M_{\odot}$ and a

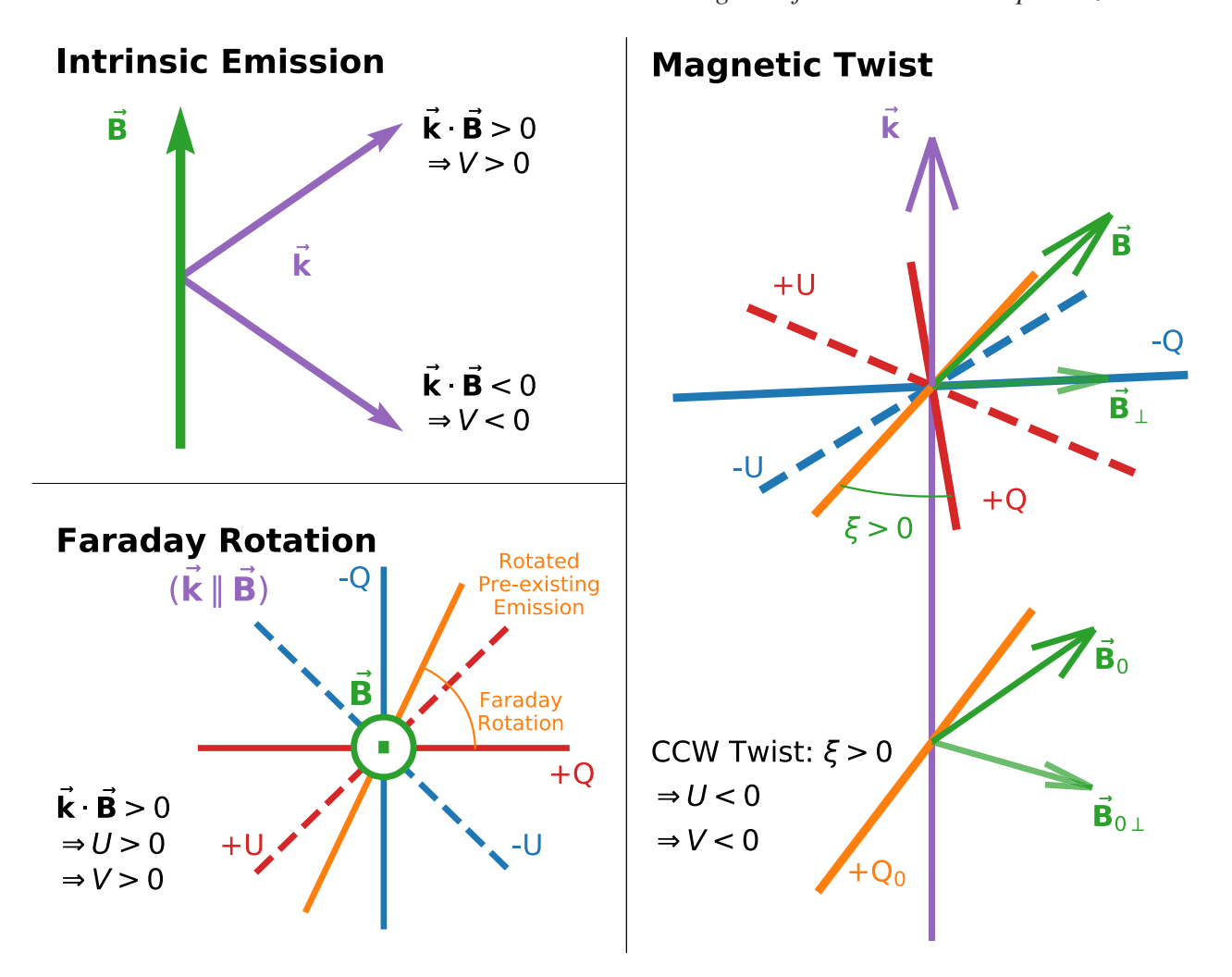


Figure 1. Schematics illustrating the mechanisms by which circular polarization can be generated and the resultant signs of Stokes V. The sign of intrinsically emitted circular polarization directly reflects the magnetic field direction with respect to the photon wavevector (top left). Intrinsically emitted circular polarization is positive if the magnetic field is pointed towards the observer, and negative if it is pointed away. Faraday conversion only operates on Stokes U, and thus Stokes V inherits the local sign of Stokes U from mediating phenomena. Circular polarization generated through Faraday conversion mediated by a small amount of Faraday rotation (bottom left) again encodes the line-of-sight magnetic field direction such that $\vec{k} \cdot \vec{B} > 0$ leads to V > 0. If the magnetic field twists along the line of sight (top and bottom right), then circular polarization generated through Faraday conversion acquires a sign opposite to the sign of the twist ξ , since it is the basis in which the Stokes parameters are defined that is twisted, rather than the emission itself. Therefore, a counter-clockwise (CCW) twist of $\xi > 0$ generates V < 0.

distance of 16.9 Mpc, consistent with stellar dynamics and shadow size measurements of M87* (Gebhardt et al. 2011; Event Horizon Telescope Collaboration 2019f). Then, we adopt the accretion rate scalings that are fit in Event Horizon Telescope Collaboration (2019e) to reproduce an average flux of 0.5 Jy at 230 GHz. Such scaling is possible because ideal GRMHD simulations are invariant under the transformation $\rho \mapsto \mathcal{M}\rho$ and $\vec{B} \mapsto \mathcal{M}^{1/2}\vec{B}$, where ρ is the mass density, \vec{B} is the magnetic field vector, and \mathcal{M} is a scalar.

3 MAGNETIC FIELD STRUCTURE

3.1 How circular polarization encodes the magnetic field

There are three pathways to generate circular polarization, each of which reflects a different aspect of the magnetic field: intrinsic emission, Faraday conversion mediated by Faraday rotation, and Faraday conversion mediated by a line-of-sight twist in the magnetic field (e.g. Wardle & Homan 2003). These processes are illustrated in Fig. 1.

First, synchrotron emission intrinsically produces a small amount of circular polarization. The sign of this circular polarization directly encodes the line-of-sight direction of the magnetic field \vec{B} with respect to the photon wavevector \vec{k} . The emitted radiation has positive V if the two vectors are aligned $(\vec{k} \cdot \vec{B} > 0)$ and negative V if they are anti-aligned $(\vec{k} \cdot \vec{B} < 0)$.

At the same time, synchrotron emission produces a large linear polarization fraction in these models, oriented as illustrated in Fig. 2. In the local plasma frame, linear polarization is initialized perpendicular to both the magnetic field and the photon wavevector, which is locally defined as the +Q direction (parallel to the electric field). As this linear polarization propagates along \vec{k} , some of it can be converted to circular via Faraday conversion. However, Faraday conversion only operates on Stokes U in the local plasma frame, a component neither parallel nor perpendicular to $\vec{k} \times \vec{B}$. If U > 0, the resulting circular polarization has V > 0, and vice versa. Since the intrinsic synchrotron emission has only +Q (i.e. U = 0), something has to recast a part of the emitted Q into U as the radiation propagates

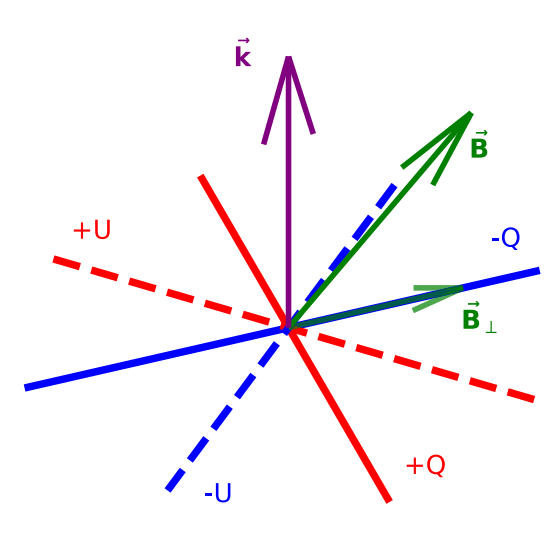


Figure 2. Schematic showing the definitions of the Stokes parameters in the local tetrad frame, defined by the photon wavevector \vec{k} and the magnetic field vector \vec{B} . Synchrotron emission produces linearly polarized emission in the +Q orientation, perpendicular to both the photon wavevector and the magnetic field.

through the plasma for Faraday conversion to occur. This can happen in two ways, corresponding to two pathways through which Faraday conversion can operate.

Faraday rotation can change the plane of polarization as the radiation propagates by directly exchanging Q and U. The sense of rotation operates via the 'right-hand rule' on the direction of the line-of-sight component of the magnetic field. For small amounts of Faraday rotation, if $\vec{k} \cdot \vec{B} > 0$, Faraday rotation converts +Q partially to +U, and Faraday conversion then creates circular polarization with +V. Similarly, $\vec{k} \cdot \vec{B} < 0$ leads to -V.

The other way in which Faraday conversion can operate is if the component of the magnetic field perpendicular to \vec{k} rotates because of a line-of-sight twist in the magnetic field. Since the basis in which the Stokes parameters are defined is tied to the local magnetic field, if the field twists along the line of sight, radiation that was initially emitted entirely as Stokes +Q can be 'recast' as partially Stokes U, with a sign depending on the direction and degree of the twist. In this pathway, since it is the polarization basis rather than the radiation itself that is rotating, a small positive (CCW) twist in the magnetic field produces -U and consequently through Faraday conversion -V.

We caution that the above discussion on the sign of V resulting from Faraday conversion applies only for small relative rotations of the plane of polarization ($<90^\circ$). For larger rotations, the sign of U generated by either Faraday rotation and/or magnetic field twist flips each time the relative polarization plane is rotated by an additional $<90^\circ$. In practice, the large Faraday rotation depth in some of these models (Mościbrodzka et al. 2017; Jiménez-Rosales & Dexter 2018; Ricarte et al. 2020) can also depolarize circular polarization in their images, by essentially randomizing the sign of U that would be converted into V, as we will further discuss in Section 4.3.

3.2 Generic magnetic field properties

Since the mechanisms to generate circular polarization depend on the details of the magnetic field, let us first explore its three-dimensional geometry. Assuming an initial dipolar magnetic field structure, frame dragging and flux freezing produce a generic helical magnetic field pattern, as illustrated in Fig. 3 (e.g. Semenov, Dyadechkin & Punsly 2004). Notice that the handedness of these helices flips across

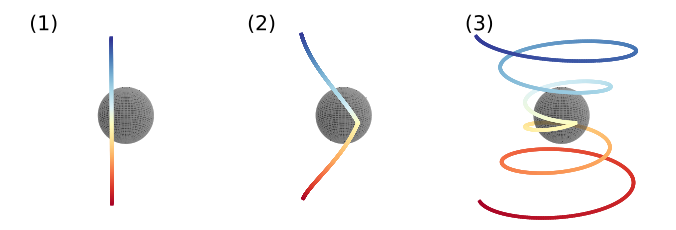


Figure 3. Cartoon illustrating the formation of a twisted magnetic field. A vertically oriented field line is twisted by frame dragging and flux freezing. Notice the opposite handedness of the twist generated above and below the mid-plane. The colours of these curves simply denote relative position along the field lines.

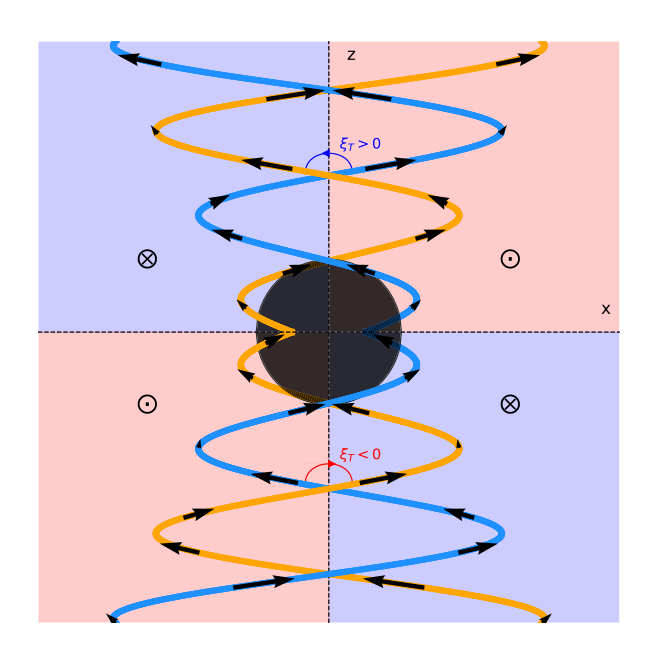


Figure 4. Schematic illustrating two field lines anchored at opposite sides of the disc mid-plane. The \bigcirc and \bigoplus symbols indicate whether the magnetic field lines move out of or into the page. Note the four quadrants generated by the sign flip in the tangential and radial components across the mid-plane, as illustrated in Fig. 3. At two locations chosen at opposite sides of the mid-plane, the angle ξ_T illustrates the magnetic twist direction between the back and front sides, what we term the 'transverse twist.' Since the top and bottom helices have opposite handedness, ξ_T flips sign across the mid-plane.

the mid-plane, resulting in a sign flip in the radial and tangential components of the magnetic field.

The outcome of this process is the structure illustrated in Fig. 4, where blue and orange curves represent magnetic field lines anchored on opposite sides of the BH in the mid-plane. We have assumed that the BH angular momentum, the disc angular momentum, and the direction of the dipolar magnetic field are all aligned with what we illustrate as the z-axis. Applying Ampere's law, this configuration corresponds to an inward current towards the BH. We comment that for a small sample of AGN with constrained jet magnetic field geometries, there does appear to be a preference for inward currents (Gabuzda 2018b) that matches expectations from the cosmic battery mechanism (Contopoulos & Kazanas 1998; Koutsantoniou & Contopoulos 2014); see Bisnovatyi-Kogan et al. (2002) and Contopoulos et al. (2018) for further discussion of the viability of the cosmic battery. For a dipolar field initialized in the positive zdirection, the field lines head out of the page in red regions marked with the ① symbol, and into the page in blue regions marked with

the \bigoplus symbol. Two sign flips occur in the line-of-sight magnetic field direction, across both the x- and z-axes in this cartoon, which is also pointed out by Tsunetoe et al. (2020b). This pattern, which we refer to as the 'four quadrants,' reverses if the dipolar field is instead initialized in the negative z direction. The sign flip across the z-axis is just a viewing angle effect due to rotation, while the sign flip across the mid-plane is physical, generated as described in Fig. 3. The mid-plane sign flip implies the existence of an equatorial current sheet, which would be subject to plasmoid instabilities and magnetic reconnection in higher resolution simulations that include resistivity (Ripperda, Bacchini & Philippov 2020).

3.3 Magnetic twist

In the absence of physical effects to exchange Stokes Q and U, the line-of-sight twist in the magnetic field determines the sign of circular polarization generated through Faraday conversion (Gabuzda et al. 2008). We write the magnetic twist along a line of sight as ξ , where a right-handed (CCW) twist has positive ξ , and a left-handed (clockwise) twist has negative ξ . Throughout this work, we always consider twist as defined in the direction of the photon's propagation, through the source to the observer.

During our explorations, we found that circular polarization generated via conversion mediated by magnetic twist could exhibit two different signs when viewing the same side of the disc tilted at different angles. This is because there are two different relevant twists, depending on one's viewing inclination, which we term the 'transverse' twist (for edge-on viewing angles) and 'vertical' twist (for pole-on viewing angles). By examining Fig. 4, we can determine the sign of what we term the 'transverse twist' of these helices, ξ_T : the relative twist between the far- and near-side magnetic field lines for this edge-on inclination. These are illustrated by the blue and red arcs in this figure. If the angular momentum of the system is oriented in the +z direction, then $\xi_T > 0$ above the mid-plane and $\xi_T < 0$ below the mid-plane. Note that the magnetic twist is invariant to the sign of the magnetic field; it would be the same if the arrows denoting the direction of the field were reversed.

We distinguish the 'vertical twist,' ξ_V , from the 'transverse twist,' ξ_T , as the twist of this structure when viewed from pole-on inclination angles. The vertical twist is more relevant for M87* than its transverse twist, since we view the system at approximately 20° inclination (Walker et al. 2018). The vertical twist direction can be deduced from generic parabolic jet structures that widen more rapidly at the base than at larger distances (e.g. Asada & Nakamura 2012; Chatterjee et al. 2019). This implies that as |z| increases, the radial component of a magnetic field threading such a structure weakens relative to its tangential component. In the funnel, it is actually the vertical field that dominates, which would go into or out of the page, but we are concerned only with the part of the magnetic field perpendicular to the propagation direction.

From this, we can infer the sign of the vertical twist, as illustrated in Fig. 5. In the z>0 region, $\xi_T>0$ but $\xi_V<0$, while the opposite is true for the z<0 region. This implies that for generic accretion flows near the event horizon, **vertical and transverse twist have opposite sign in the same region**. When viewing the same side of the disc edge-on, the transverse twist is more important for determining

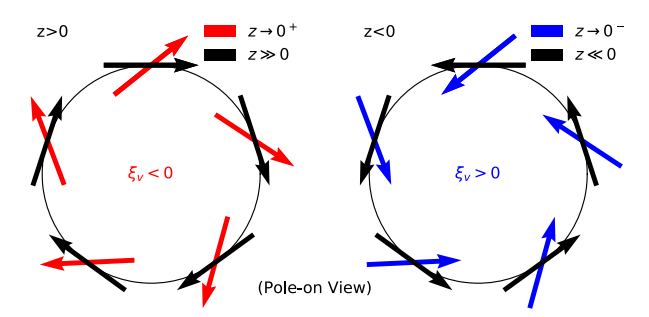


Figure 5. Schematic illustrating vertical twist, ξ_V , for a pole-on viewing angle. Here, the angular momentum of the BH is in the positive z direction, out of the page. Because parabolic jets radially expand more rapidly near the base than at large distances, the radial component of a magnetic field threading such a structure grows weaker relative to the tangential component as |z| increases. Interestingly, comparing ξ_V to ξ_T in Fig. 4, the vertical twist in a given physical region exhibits the opposite sign as its transverse twist.

circular polarization, while for pole-on inclination angles, the vertical twist is more important. We confirm the sense of vertical twist in our GRMHD models in Appendix A.

3.4 Magnetic fields of our GRMHD models

Next, we examine the magnetic field structure of our two GRMHD models to learn how they may depart from the simple pictures described in the previous section. In Fig. 6, we plot the magnetic fields in the coordinate frame in Cartesian Kerr-Schild coordinates. These are decomposed into their radial, azimuthal, and vertical components, then azimuthally averaged during the final snapshot, time t = 10000 $GM_{\bullet} c^{-3}$. These decompositions are normalized to the local magnetic field strength, such that $\langle B_{\text{tot}} \rangle^2 = \langle B_r \rangle^2 + \langle B_\phi \rangle^2 + \langle B_z \rangle^2$. There are three interesting phenomena to notice in this figure. First, these two models generally have stronger azimuthal fields than radial fields, which need not generally be true. The azimuthal component dominates everywhere except in the funnel, directly above and below the BH. Secondly, notice the sign flip in the radial and tangential field components as discussed in the previous section. Thirdly, the SANE model is more turbulent and disordered than the MAD model, complicating the simple picture drawn in Fig. 4. This turbulence will appear as noise in its circular polarization images.

By performing path integrals on the magnetic field (in Cartesian Kerr–Schild coordinates), we produce three-dimensional visualizations using VISIT, shown in Fig. 7 (Childs et al. 2012). Magnetic field lines coloured blue are anchored within the plane of the disc, while magnetic field lines coloured red are anchored around the BH (on a sphere of radius 2 $GM_{\bullet}\,c^{-2}$). The left column depicts the MAD simulation, while the right column depicts the SANE simulation. In both cases, the magnetic field in the funnel region is ordered and well defined. However, the disc magnetic field in the MAD model is more ordered and has a stronger vertical component than its SANE counterpart. These visualizations also reveal a steep pitch angle in the funnel region that affects the circular polarization produced by the transverse twist (e.g. Gabuzda et al. 2008).

4 CIRCULAR POLARIZATION IMAGES

4.1 Circular polarization in our models

In Figs 8 and 9, we introduce the circular polarization images of the MAD and SANE models, respectively. The top row plots a pole-on viewing angle of 5°, while the bottom row plots an edge-on

¹To be more explicit, the magnetic twist along the photon trajectory between points A and B is the angle, in the plane perpendicular to the photon wavevector at point B, between the local magnetic field vector and the vector resulting from parallel transport of the magnetic field vector from point A to point B.

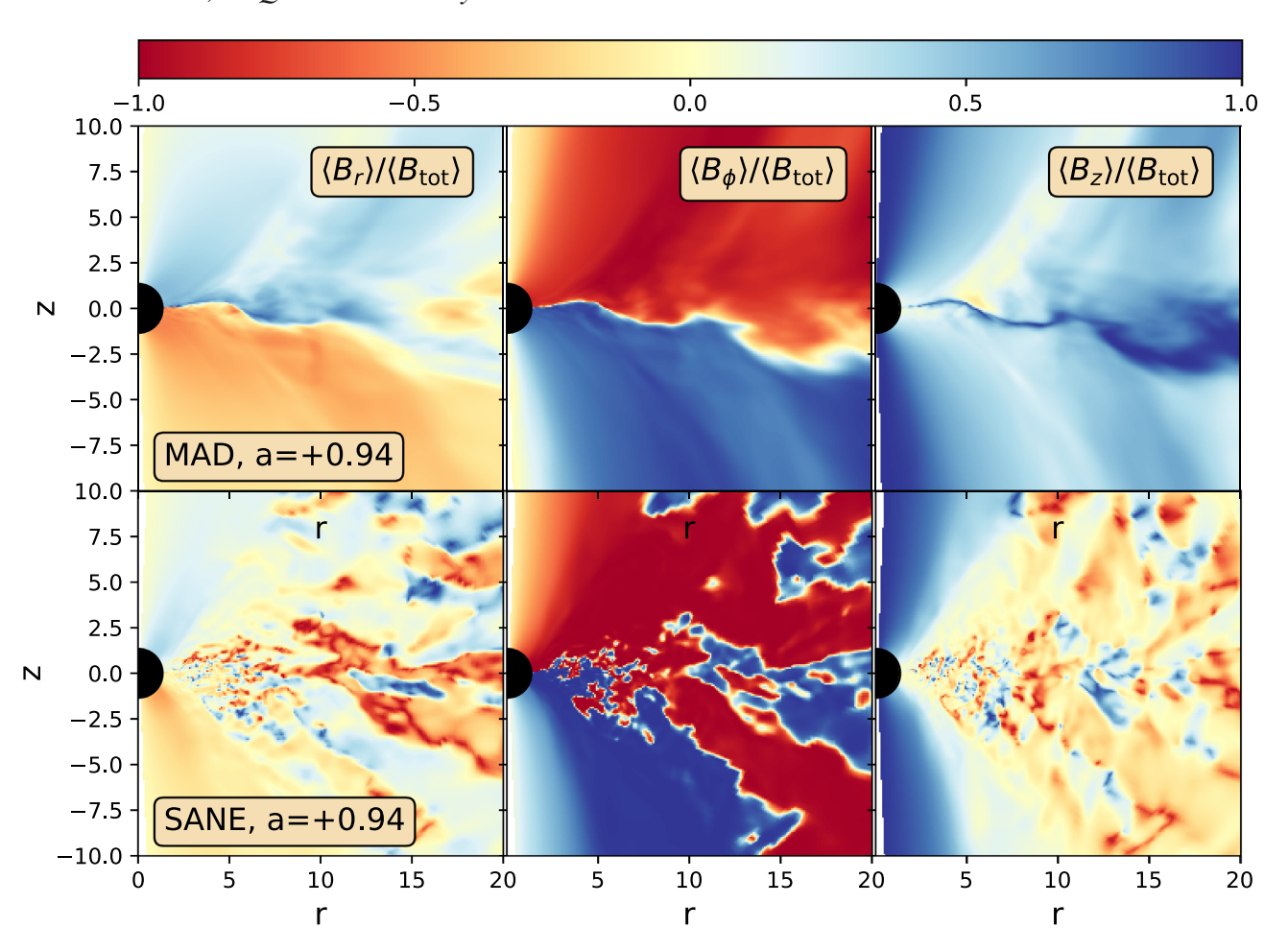


Figure 6. Azimuthally averaged magnetic field decompositions in the coordinate frame for the two models explored in this study during their final snapshots. Notice (i) the dominance of the azimuthal field component in these particular models, (ii) the sign flip in the azimuthal and radial components across the mid-plane, and (iii) the greater disorder in the SANE model compared to the MAD.

viewing angle of 90°. For these figures alone, we have time-averaged 501 images, one for each of the snapshots in the final quarter of the simulation, $7500 < GM_{\bullet} c^{-3} < 10\,000$. Time-averaged circular polarization images (Stokes V) are shown in the first column, the image of just the final snapshot is shown in the second column, and the circular polarization fraction (Stokes V/I) is shown in the third column. Immediately we can see that images from both models and both viewing angles feature both positive and negative regions, which will complicate the interpretation of the unresolved Stokes V measurements. The face-on MAD image is surprisingly dominated by its photon ring (discussed at length in Section 4.3.2), while the edge-on images are preferentially dominated by opposite signs of circular polarization on opposite sides of the mid-plane.

Comparing the two, the MAD image appears more ordered than its SANE counterpart. Furthermore, the photon ring, prominent in the face-on MAD circular polarization image (and discussed at length in Section 4.3.2), is suppressed in the SANE image. Some of the disorder in the SANE is due to its more turbulent magnetic field structure, as shown in Fig. 6. Moreover, the SANE model is more scrambled by its much larger Faraday rotation and conversion depths. Further discussed in Section 4.4, the much higher Faraday conversion depth in the SANE model also leads to a much larger fractional circular polarization (see also Event Horizon Telescope Collaboration 2021b). We plot the Faraday depths of these models in Fig. 10, where the Faraday rotation depth $\tau_{\rho_V} = \int \rho_V ds$ and the

Faraday conversion depth $\tau_{\rho Q} = \int \rho_Q ds$. Here, ρ_V and ρ_Q are the radiative transfer coefficients responsible for Faraday rotation and conversion, respectively (see Dexter 2016; Mościbrodzka & Gammie 2018 for more details). In this figure, the brightness of each pixel encodes its total intensity, while the colour encodes the appropriate Faraday depth as indicated in the colour bar. The intensity-weighted image average of these values is written on the bottom of each panel. The top row shows an inclination of 5° , while the bottom row shows an inclination of 90° . In Appendix B, we decompose the emissivity and rotativity along the lines of sight marked by white circles in this figure.

At 5° , the MAD model is both Faraday rotation and conversion thin, while the SANE model is strongly Faraday rotation thick and moderately Faraday conversion thick. Faraday rotation is directly encoded in the rotation measure, which for M87* has been observed to have a magnitude of $\approx\!10^5$ rad m $^{-2}$ and exhibit sign flips (Goddi et al. 2021), consistent with GRMHD studies (Ricarte et al. 2020). At an inclination of 90° , the MAD model becomes moderately Faraday rotation thick, while the SANE becomes thick to both Faraday rotation and conversion. We should thus expect that the circular polarization of the MAD model should more closely reflect the simple and ordered magnetic field structure discussed in Section 3.

Now, to understand the features of these images in detail, we will decompose their circular polarization images into components originating from intrinsic emission and Faraday conversion, and

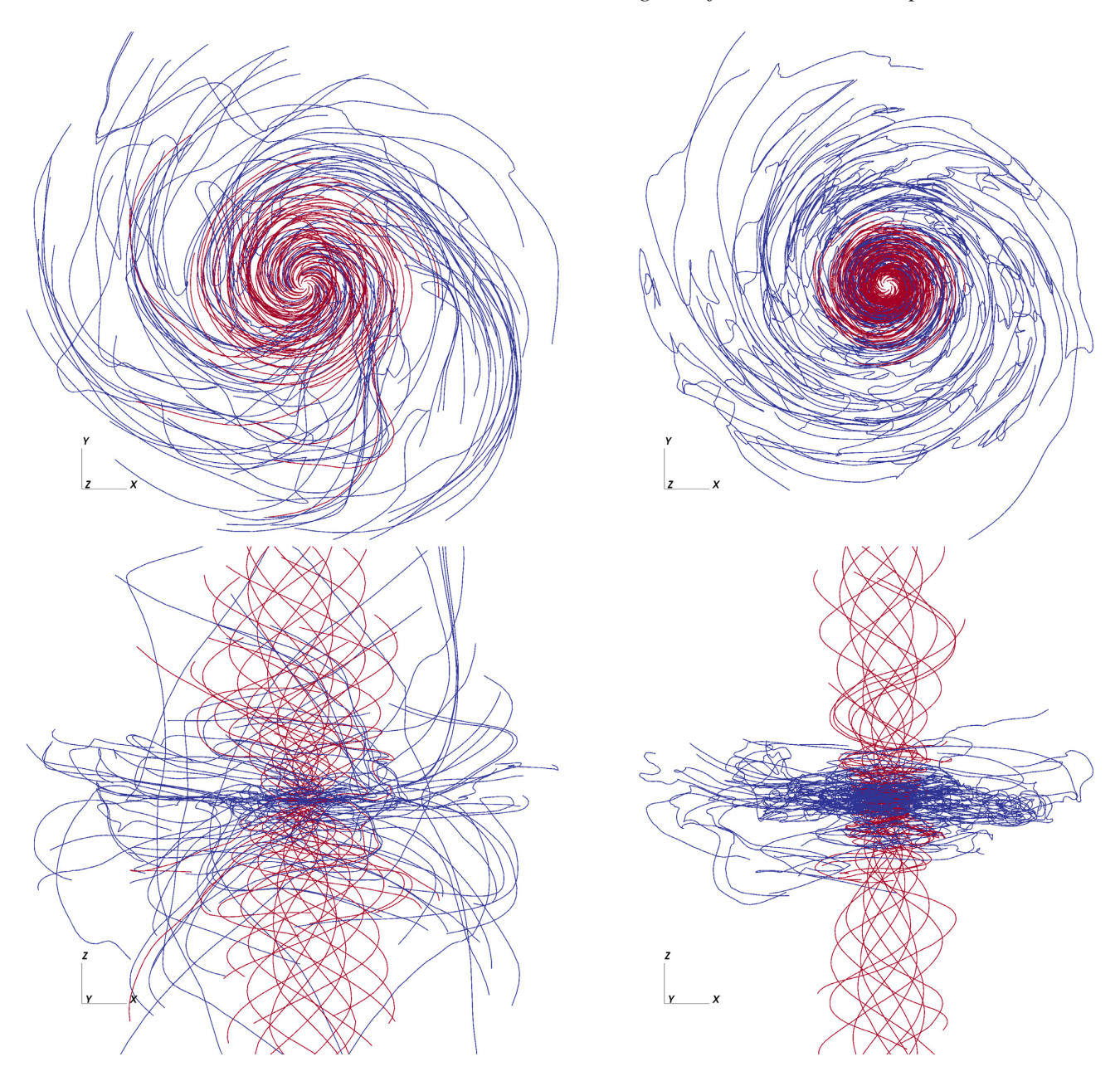


Figure 7. Magnetic field line illustrations created with VISIT by integrating magnetic field components in Cartesian Kerr–Schild coordinates. The MAD $a_{\bullet} = +0.94$ simulation is visualized in the left column, while the SANE $a_{\bullet} = +0.94$ simulation is visualized in the right column. Lines coloured red are anchored to a sphere of radius $2 GM_{\bullet} c^{-2}$, while those coloured blue are anchored to a disc in the mid-plane. The fields in the jet funnel are similar in both models, but the disc field is more ordered and has a stronger vertical component in the MAD model.

explore how the sign of the circular polarization encodes the magnetic field geometry.

4.2 Intrinsic emission

To generate images of purely intrinsic emission, we remove Faraday conversion effects from IPOLE by setting the radiative transfer coefficient $\rho_Q=0$. Without conversion, linear polarization cannot be transformed into circular, and the only remaining mechanism for the production of circular polarization is intrinsic synchotron emission. Recall that the sign of the intrinsic emission encodes the direction of the line-of-sight magnetic field.

4.2.1 Edge-on – four quadrants

The geometry imprinted on to the intrinsic circular polarization is most clearly seen in the circular polarization fraction, *VII*. This is plotted for our two models in Fig. 11 for an edge-on viewing angle. We see the 'four quadrants' pattern of the magnetic field geometry as described in Fig. 4. Recall that the sign flip across the *z*-axis is due to the helical twisting of field lines, while the sign flip across the mid-plane is physical. The intrinsic circular polarization fraction can reach a few per cent in some areas. However, circular polarization generated via intrinsic emission is sub-dominant in the bright parts of the image compared to that generated by Faraday conversion in these particular models, as we will explore in more detail in Section 4.4. In addition, we notice substantial cancellation due to

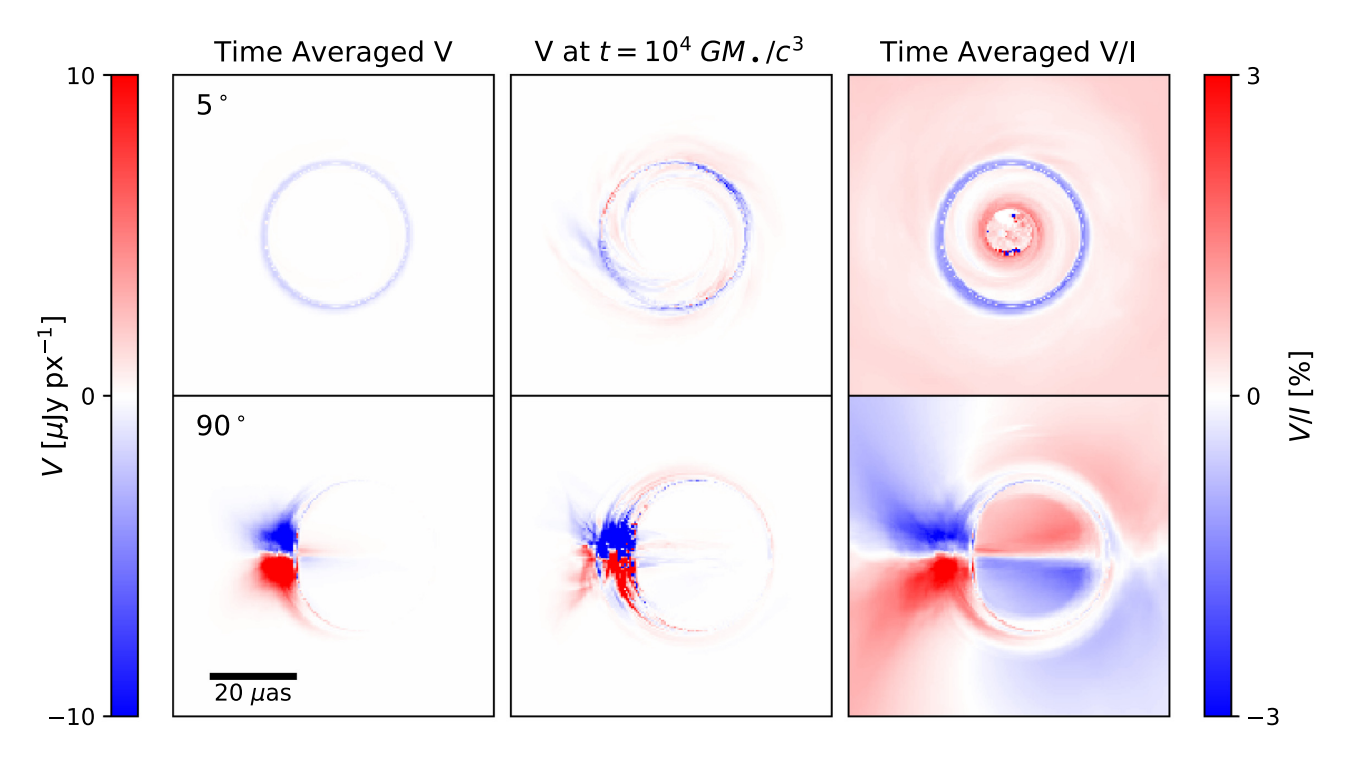


Figure 8. An introduction to the circular polarization of our MAD model. The final snapshot ($t = 10\,000\,GM_{\bullet}\,c^{-3}$) is shown. The top row displays the system with a pole-on inclination of 5°, while the bottom row displays the system at an edge-on inclination of 90°. In the first and third columns, 501 images between $7500 < GM_{\bullet}\,c^{-3} < 10\,000$ have been averaged. In the centre column, we display the final snapshot. For this model, the photon ring dominates the circularly polarized image for pole-on inclinations, while a sign flip across the mid-plane that reflects a sign flip in the 'transverse twist' is seen at edge-on inclinations.

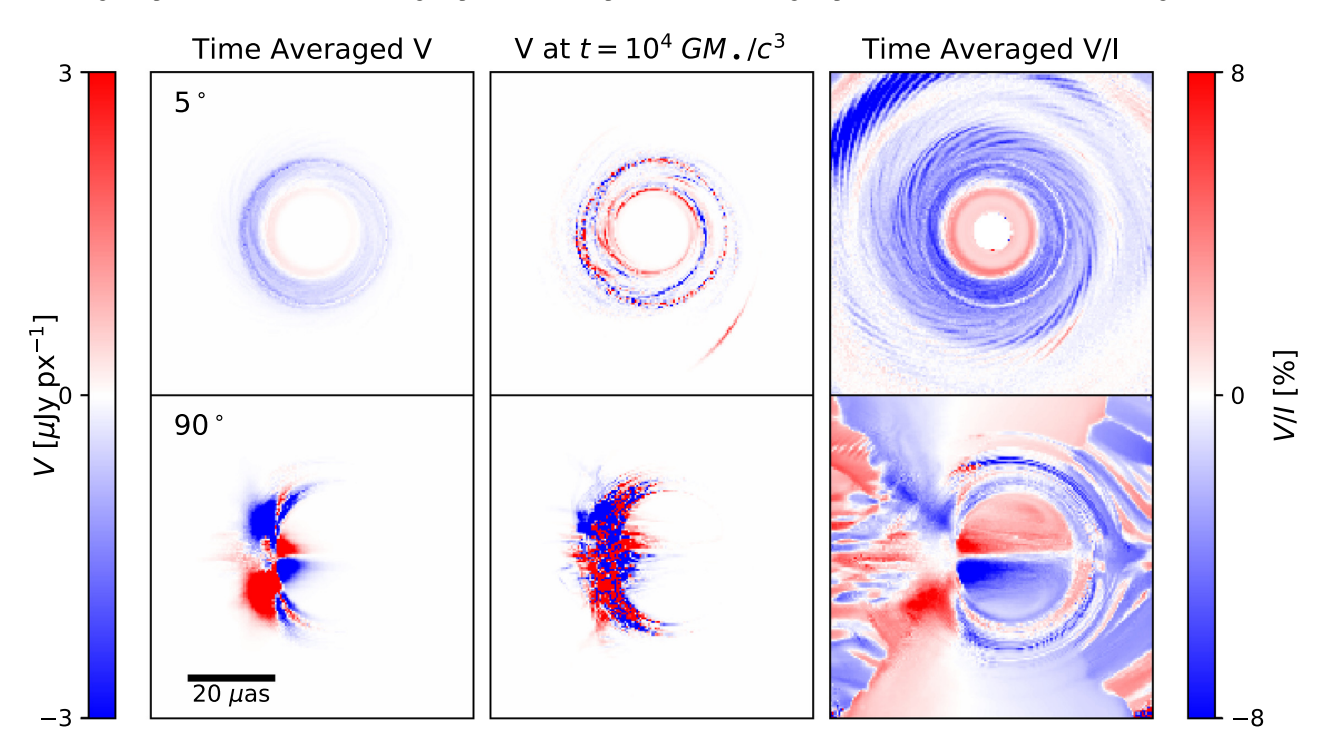


Figure 9. As Fig. 8, but for the SANE model. At a given snapshot, the SANE model image is messier than the MAD's due to both its more turbulent disc and its higher Faraday depths. Faraday rotation scrambles the photon ring more strongly in this model. Note the different colour scalings for this figure compared to Fig. 8.

the symmetry of these images. The 'four quadrants' pattern is also discussed in Tsunetoe et al. (2020b), who find that the leftward offset of the vertical sign-flip from the centre of the image is due to beaming effects. Ricarte et al. (2020) discuss the potential impact

of bandwidth depolarization in images of Faraday thick models. To ensure that bandwidth depolarization does not significantly impact our images, we average 129 individual images within a bandwidth of 4 GHz in Figs 11, 12, and 13. We found that bandwidth averaging

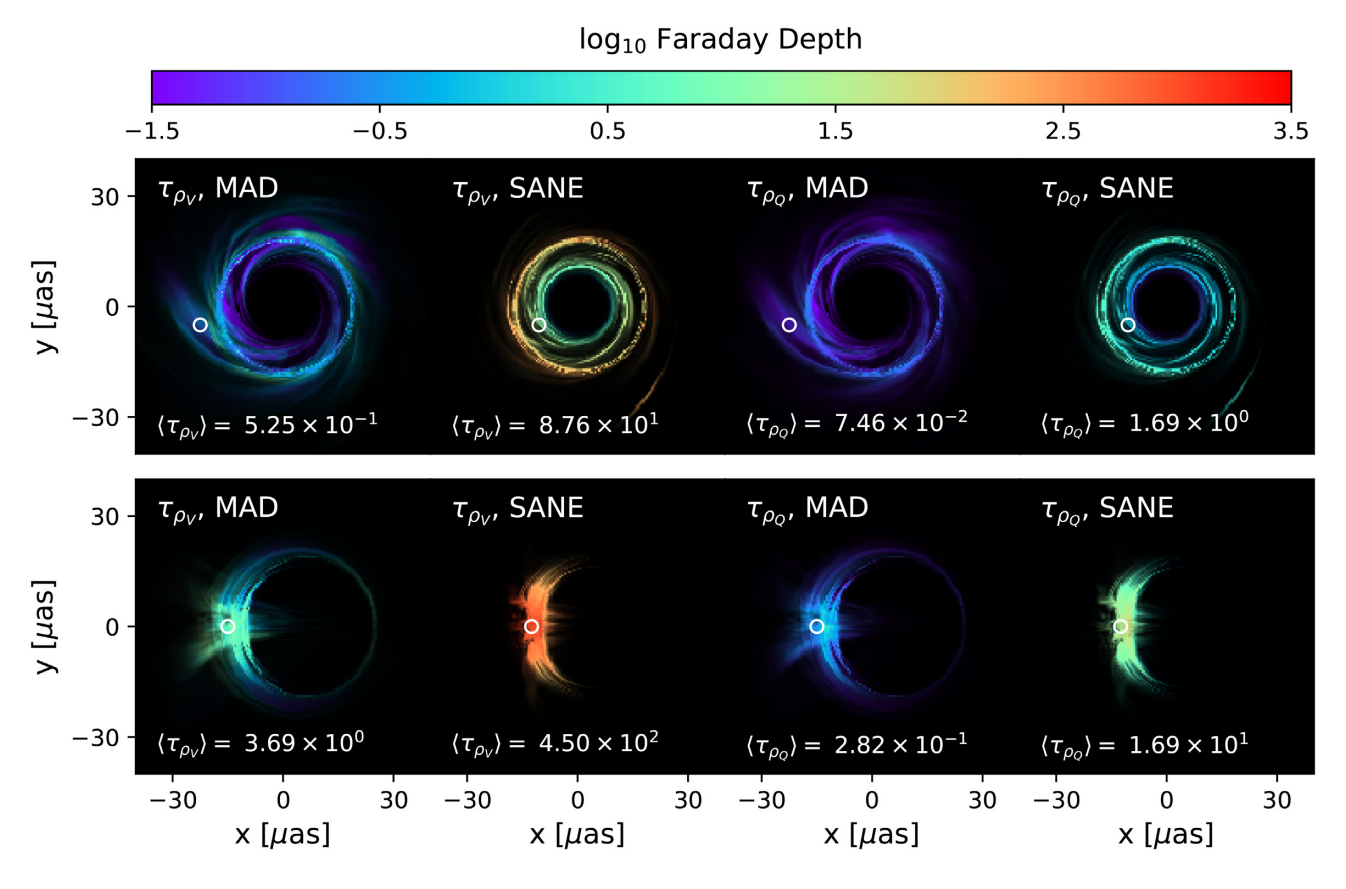


Figure 10. Depths of Faraday rotation (τ_{ρ_V}) and conversion (τ_{ρ_Q}) in our models when viewed at 5° (top row) and 90° (bottom row). The MAD model is more Faraday thin than the SANE model. Both models are more thick to Faraday rotation than Faraday conversion. Models are more Faraday thick for edge-on inclinations than face-on ones. In the pixels marked with white circles, we study the emissivity and rotativity along the line of sight in Appendix B.

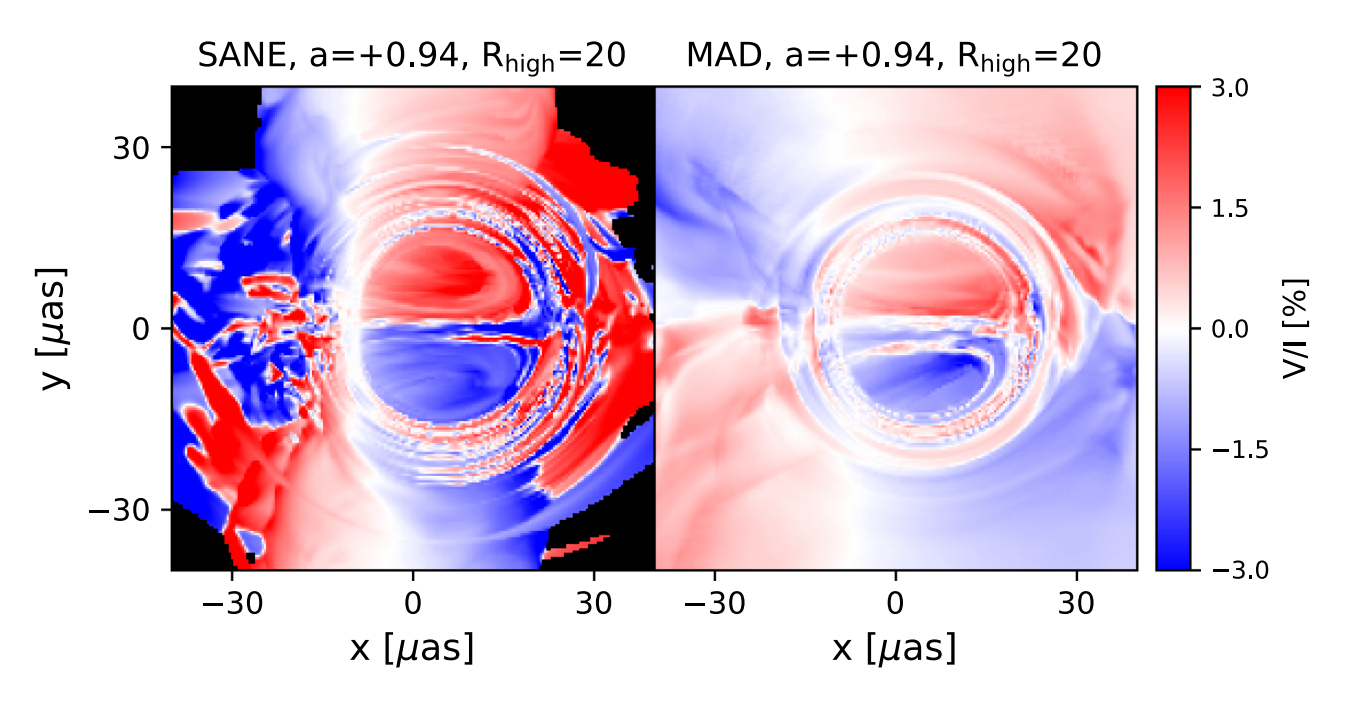


Figure 11. Intrinsic circularly polarized emission fractions (Faraday conversion switched off) for our two GRMHD models, viewed edge-on. We see the 'four quadrants' pattern resulting from the magnetic field geometry shown in Fig. 4. Intrinsic emission dominates the circular polarization on large scales, producing a diffuse background.

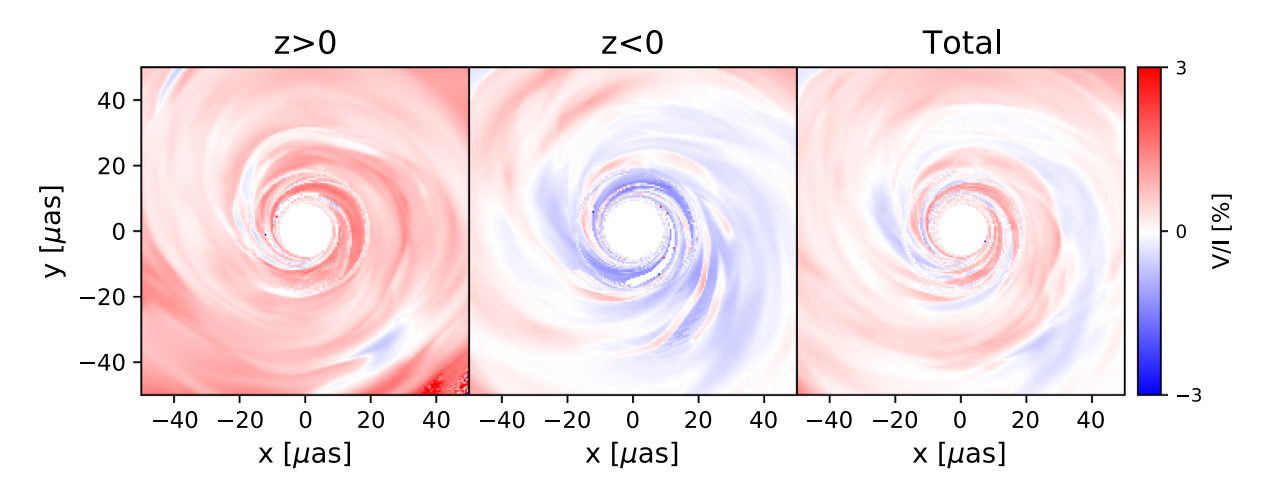


Figure 12. Intrinsic circularly polarized emission fractions (Faraday effects switched off) for the MAD model, viewed face-on. One might expect a single sign of the circular polarization, corresponding to the vertical field direction. Instead, we find a sign flip for emission originating on the far side of the mid-plane. This is due to the inward bending of photon orbits, causing the circular polarization to be sensitive to the radial magnetic field in addition to the vertical component. For the magnetic field geometry described in Section 3, the radial field on the far side of the BH always has the opposite sign as the vertical field.

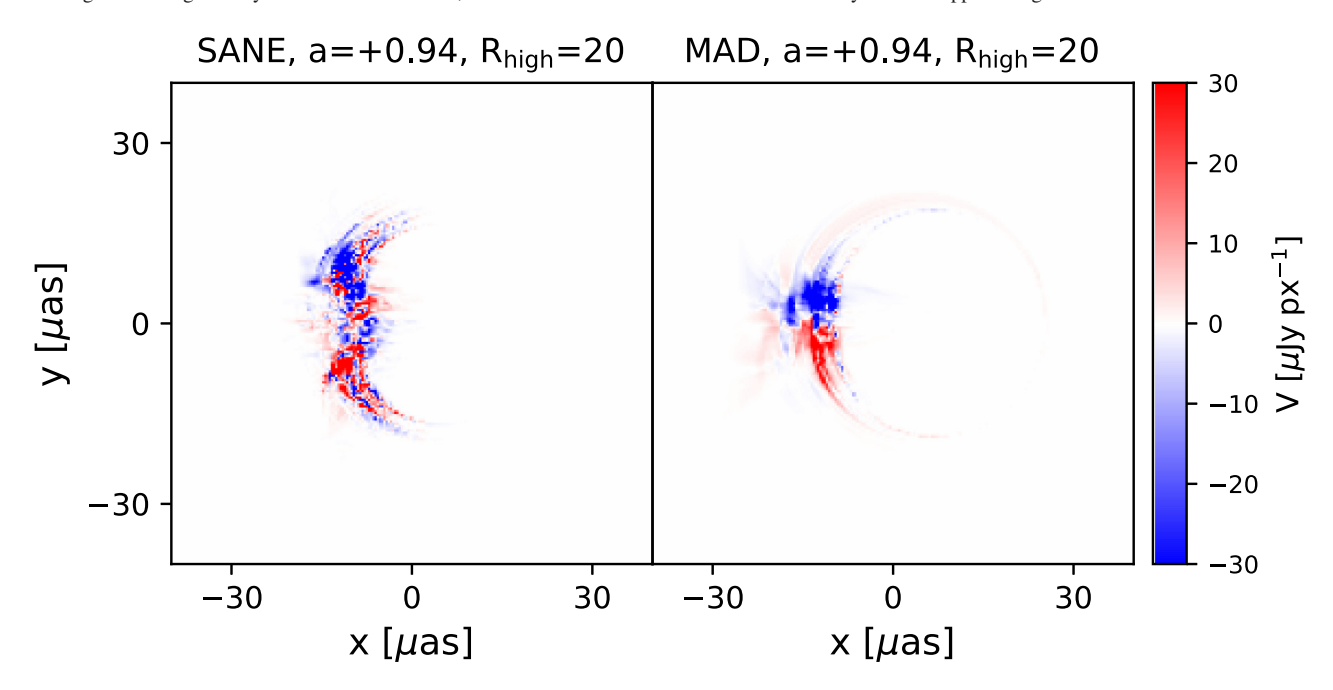


Figure 13. Circular polarization images of our two models, purely from Faraday conversion, $j_V = 0$, from an edge-on viewing angle. These images are very similar to the lower central panels of Figs 8 and 9, because Faraday conversion dominates the circular polarization in the bright parts of the image. Both images are predominantly negative on top and positive on the bottom, directly reflecting the direction of transverse twist shown in Fig. 4.

has negligible effect on these images, owing in part to the relatively small value of R_{high} adopted.

4.2.2 Face-on – B_z , plus B_r on the far side

For face-on inclinations, one might expect to see only a single sign of intrinsic circular polarization, corresponding to the direction of the vertical magnetic field, B_z . Instead, as plotted in Fig. 12, we find that the intrinsic emission from the far side of the emitting region, behind the mid-plane, tends to exhibit the opposite sign. This unanticipated phenomenon is due to the lensing of photon orbits. Behind the mid-plane, photon orbits are bent towards the BH, causing the circular polarization to be sensitive to not only the vertical magnetic field, but also its radial component. Assuming the geometry sketched in

Fig. 4, B_r on the far side always has the opposite sign of B_z . Flips in the apparent line-of-sight direction of the magnetic field have also been found in these models in the context of Faraday rotation, which similarly encodes the direction of the magnetic field relative to the photon wavevector (Ricarte et al. 2020).

4.3 Faraday conversion

Faraday conversion exchanges linear and circular polarization states. On its own, it is insensitive to the sign of the magnetic field, and depends on the relative twist between the field producing the emission and the field performing the conversion. We create images of circular polarization due only to Faraday conversion by switching off the coefficient responsible for intrinsic emission, $j_V = 0$. In

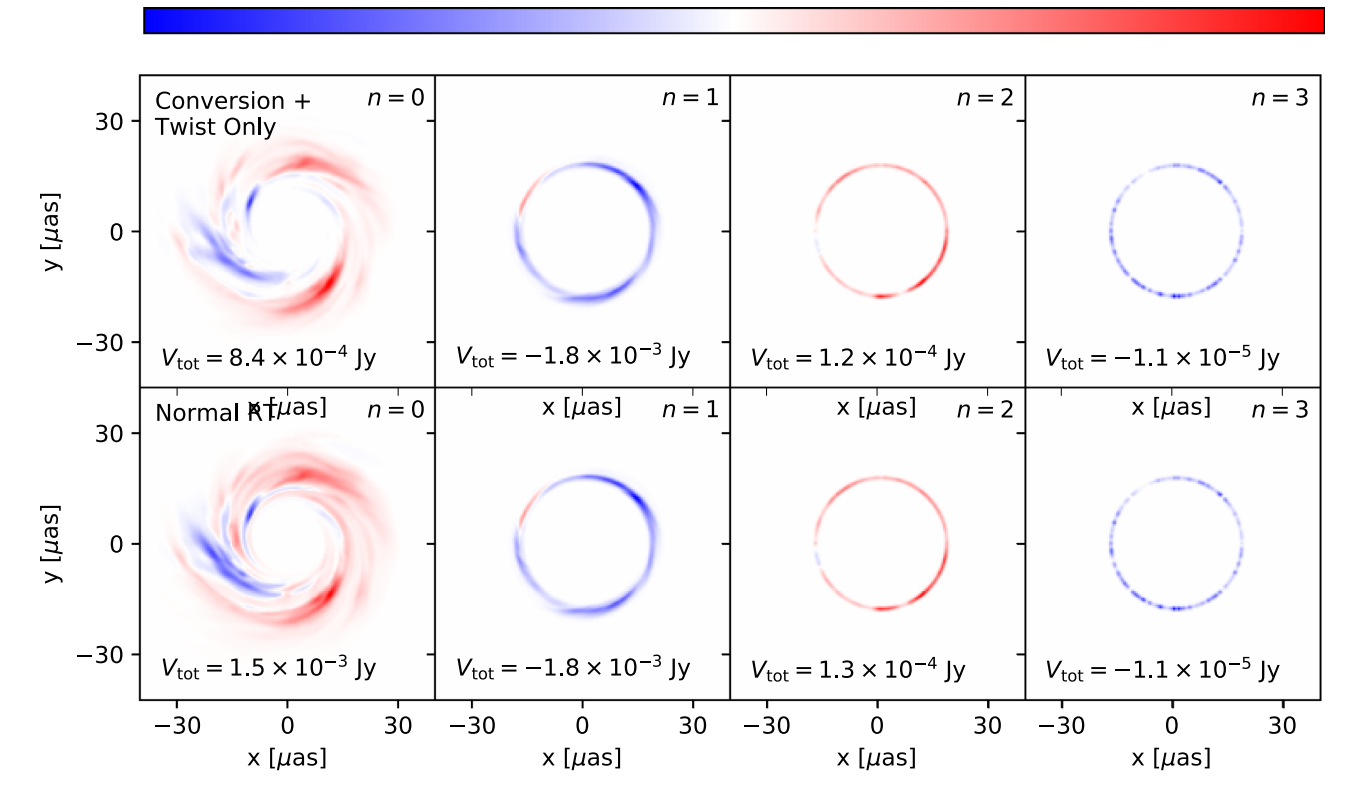


Figure 14. Circular polarization images of the MAD, $a_{\bullet} = 0.94$, $R_{\text{high}} = 20$ model, broken into sub-ring components, revealing that alternating sub-rings flip sign. We scale each panel's colour map individually such that the colours span $\pm \max |V|$. On the top row, only circular polarization originating from Faraday conversion through the magnetic twist pathway is plotted, by setting the radiative transfer coefficients $\rho_V = j_V = 0$. All coefficients are active in the second row, demonstrating that Faraday conversion mediated by magnetic twist causes this signal. Images are blurred with a Gaussian with a full width at half-maximum of 1 μ as to better visualize the narrow and faint sub-rings. Rings of increasing order alternate sign due to parallel transport and generic properties of the magnetic field geometry. Under the right conditions, the circular polarization of the photon ring directly encodes the handedness (vertical twist) of the magnetic field. All sub-images flip sign if the system is viewed from the opposite inclination, where the twists of the helices are reversed.

these particular models, Faraday conversion contributes more to the unresolved circular polarization image than the intrinsic emission, which we will further explore in Section 4.4.

4.3.1 Edge-on – transverse twist

For edge-on inclinations, the sign of the circular polarization encodes the transverse twist, ξ_T . As illustrated in Fig. 4, ξ_T flips sign at the mid-plane and depends on the direction that the magnetic field is twisted. Circularly polarized intensity images created only by Faraday conversion are shown in Fig. 13. These Stokes V images are predominantly negative on top and positive on the bottom, as expected from the sign of ξ_T . The SANE image is much messier due to both turbulence in the magnetic field and its thickness to both Faraday rotation and conversion. Given a circularly polarized image of an edge-on system, we expect a sign flip at the mid-plane and for the signs to directly encode the handedness of the magnetic field on either side.

4.3.2 Face-on — Vertical twist and a photon ring signature

For face-on viewing angles, circular polarization is sensitive to the vertical twist, ξ_V , which happens to have the opposite sign as the transverse twist. In the MAD model, we notice the remarkable feature that the photon ring has the opposite sign compared to the rest of the

image, a feature also discussed in Moscibrodzka et al. (2021) for a different set of MAD simulations. In fact, we find that photon subrings of increasing order alternate sign. In Fig. 14, we break down the image of the final snapshot of this model into its photon ring components (Wong, private communication). To isolate the effect of Faraday conversion mediated by magnetic twist, Faraday rotation and intrinsic emission are turned off in the top row, but normal radiative transfer is performed in the bottom row. In these panels, ncorresponds to the number of times the photon orbit has reached an extremum in the θ coordinate, counting the number of half-orbits the photon completes. The total integrated Stokes V for each sub-image is written on the bottom left. Notice that the n = 0 direct image has about a factor of two greater circular polarization when all coefficients are turned on compared to the pure conversion and twist image. This behaviour matches expectations from a magnetic field pointed towards the observer, as we will further explore in Section 4.4. For the photon ring and its sub-rings, $n \ge 1$, Faraday conversion mediated by magnetic twist completely explains the signal. Remarkably, the n = 1 photon ring dominates the circularly polarized image in this model, even though it contributes to only 16 per cent of the total (unpolarized) flux, and we confirm this to be generally true for snapshots in times $7500 < GM_{\bullet} c^{-3} < 10000$. As has been shown in previous works, photon rings of increasing order have intensities that decrease by about an order of magnitude with each half-orbit (Johnson et al. 2020; Himwich et al. 2020), but the flips in the sign of Stokes V are unanticipated.

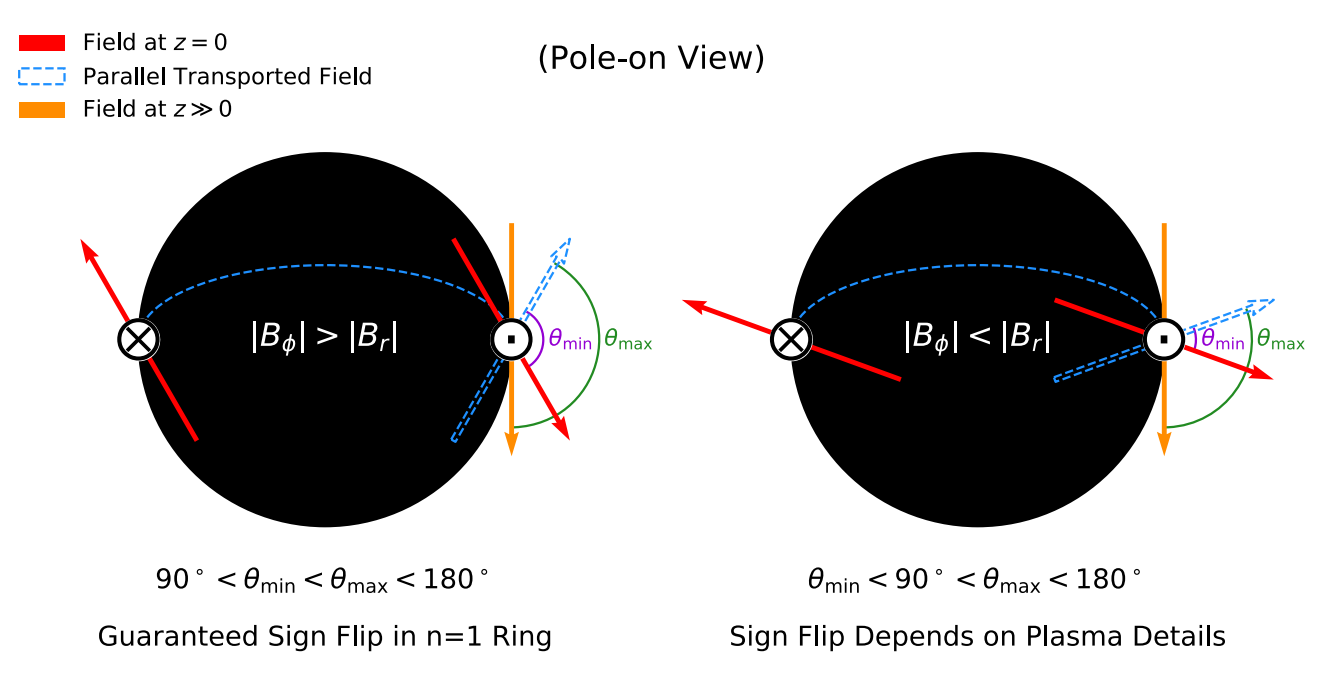


Figure 15. Schematic explaining the sign flips in the photon ring for a face-on viewing angle due to magnetic field symmetries and parallel transport. Here, we consider a pixel on the right side of the photon ring (where the arrows intersect). The magnetic field in the mid-plane is shown in red, while the field at $z \gg 0$ (towards the camera) is shown in orange. (These are the magnetic fields depicted in Fig. 5.) Emission in the n=1 photon ring is loaded on the opposite side of the BH, so to determine the line-of-sight twist, we parallel transport the emitting field along a photon geodesic around the SMBH, as illustrated in blue. The sign of Stokes V depends on the angle that this emitting field makes with the converting field ahead of it, and this is bracketed by θ_{\min} and θ_{\max} . For a toroidally dominated field (left), these angles are always confined to the quadrant between 90° and 180° , which guarantees a sign flip in the n=1 ring. This is not the case for a radially dominated field (right), so the existence of a sign flip depends on exactly where along the line of sight the Faraday conversion occurs. Faraday rotation can also disrupt these inequalities and corrupt this signal.

These sign flips can be explained by a combination of symmetries of the magnetic field, the dominance of its azimuthal component, and features of parallel transport. We illustrate how this results in a sign flip in the photon ring in Fig. 15. We consider a pole-on viewing angle and a pixel that appears in the right side of the photon ring (at the intersection of the arrows). By construction, intensity in the n=1 photon ring component originates from the opposite side of the SMBH, having bent around the back side (behind the page). The field in the mid-plane is represented by red arrows, while the field at $z \gg 0$ (towards the observer) is represented by the orange arrow. The field at $z \gg 0$ is twisted following the rules described in Fig. 5. In the left-hand panel, the magnetic field is toroidally dominated (as in our models), while in the right-hand panel, the field is radially dominated.

To determine the magnetic twist along this bent trajectory, we must parallel transport the emitting field (on the left, moving in the \bigotimes direction) along the geodesic to the converting field (on the right, moving in the \bigodot direction). When parallel transported around the back of the SMBH, the azimuthal component of the magnetic field flips sign, but the radial component does not. The relative twist between photons loaded on the left side of the SMBH and the Faraday converting material on the right side can be inferred by comparing the parallel transported field line (as shown in blue) with the field orientations both in the mid-plane (red) and at larger distances towards the camera (orange). We can see that this brackets the twist angles θ_{\min} (at the mid-plane) and θ_{\max} (at infinity).

Next, recall that Stokes V inherits the sign of Stokes U, and Stokes U depends on the relative twist between the emitting field and the

converting field. In the plasma frame, synchrotron emission produces light polarized in the +Q orientation, but a twist in the magnetic field in the propagation direction can recast what was once entirely +Q into some parts $\pm U$. Most importantly, the resultant sign of U flips each time the twist increases by 90° . For the toroidally dominated field on the left, the twist angle is always between 90° and 180° . Therefore, the n=1 photon ring should always exhibit the opposite sign of Stokes V compared to the n=0 image overall. Generalizing to n>1, emission in odd numbered sub-rings is generated on the left side of this schematic, while emission in even numbered sub-rings is generated on the right side. Consequently, odd numbered and even numbered sub-rings should each share signs.

If the field is radially dominated, as shown on the right, then unfortunately the sign of the photon ring depends on the details of the plasma. Parallel transported around the SMBH, the magnetic field would intersect the magnetic field near the mid-plane at an angle $\theta_{\rm min} < 90^{\circ}$, but would eventually encounter magnetic field where the relative angle $\theta_{\rm min} > 90^{\circ}$. The resultant sign of the circular polarization then depends on where exactly the Faraday conversion occurs along this trajectory.

To summarize, for face-on viewing angles, the sign of circular polarization of the photon ring can directly encode the handedness (the vertical twist) of the magnetic field in the approaching helix. If viewed from the opposite inclination, all sub-images would flip sign, since the handedness of the field flips across the mid-plane. As long as Faraday rotation is weak, sign flips in Stokes V are guaranteed in sub-images of increasing sign for toroidally dominated fields, and may also occur in radially dominated fields depending on the plasma details. This signal can be explained by generic properties of the magnetic field geometry, the sensitivity of circular polarization to both the direction and degree of magnetic twist, and features of

²For spinning SMBH, a photon will also move in the azimuthal direction, but due to the axis symmetry of the problem, this has no effect on our argument.

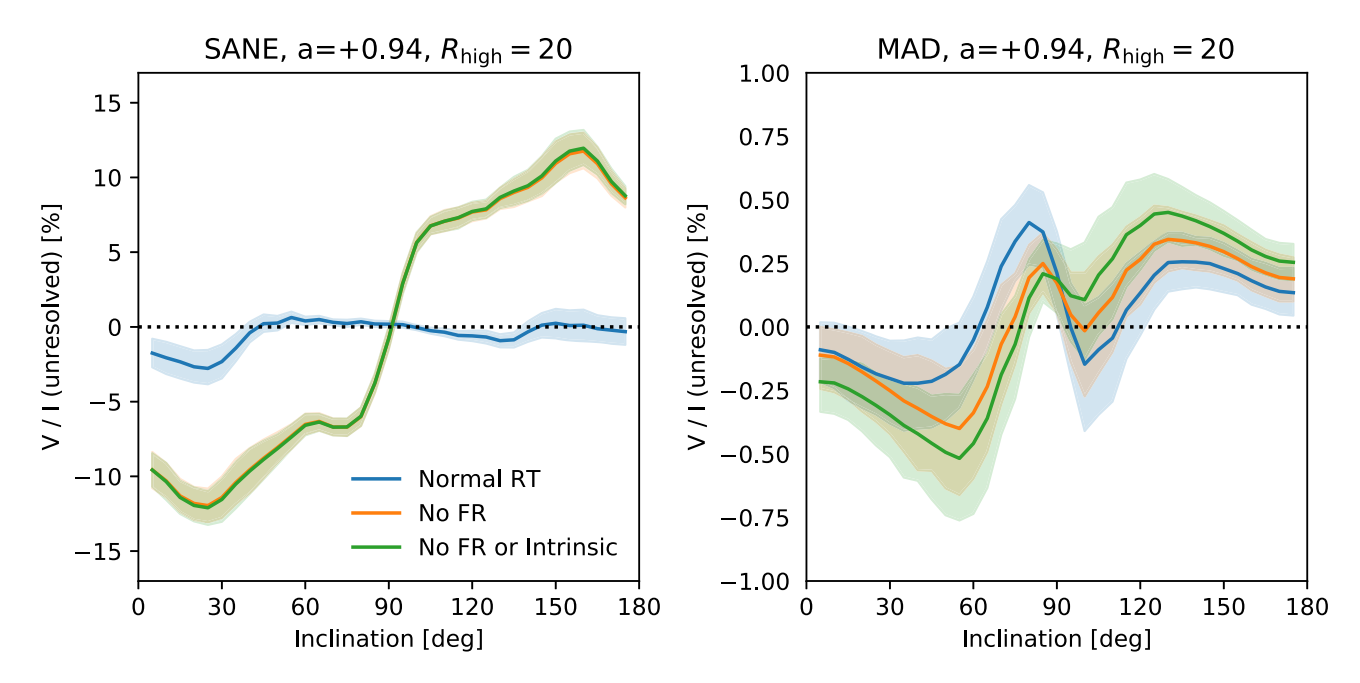


Figure 16. Image-integrated circular polarization fractions as a function of inclination for our two models. Normal radiative transfer is plotted in blue, images created without Faraday rotation are plotting in green. We include multiple snapshots in this plot, and the filled regions enclose the 5th to 95th percentiles of the values spanned between times $t \in [7500, 10\,000]~GM_{\bullet}~c^{-3}$, while the solid lines mark the median. This reveals that constancy of the sign of V/I occurs at some, but not all, inclinations. These models exist in two different regimes of Faraday rotation. In the SANE model, Faraday rotation is strong enough to significantly depolarize the circularly polarized image, while in the MAD model Faraday rotation is weak enough to imprint the magnetic field direction on the sign of V/I, pushing it towards positive values for inclinations $<90^{\circ}$ and towards negative values for inclinations $>90^{\circ}$. Intrinsic emission imprints the line-of-sight direction of the magnetic field in a similar fashion.

parallel transport within the photon ring. *EHT* imaging constraints favour clockwise rotation of material in the accretion flow of M87* (Event Horizon Telescope Collaboration 2019e). If the accretion flow is produced by a prograde model with $|B_{\phi}| > |B_r|$, then the photon ring should have V > 0. If the accretion flow is retrograde, we anticipate additional complications, as we discuss in Section 5.3.

If Faraday rotation is strong, it can corrupt this signal in two ways. First, Faraday rotation along the line of sight can further rotate the plane of polarization based on the line-of-sight magnetic field direction, potentially disrupting the inequalities in Fig. 15. Indeed, we caution that for our Faraday rotation thick SANE model, we only see the signal exactly as described in this section if Faraday rotation is switched off. Secondly, strong enough Faraday rotation can scramble the circular polarization by randomizing the sign of Stokes *U* that gets converted to *V*, which especially affects photon ring geodesics, since they have larger than usual path lengths through the system. Complementary linearly polarized images, especially at multiple frequencies, would help assess if Faraday rotation in the photon ring is important.

4.4 Unresolved circular polarization measurements

The sign of unresolved circular polarization measurements has been proposed to infer the sense of rotation in quasar engines (Enßlin 2003). Using our two models, we probe to what extent the unresolved circular polarization fraction and its time variability can be used to infer the magnetic field geometry on event horizon scales. In Fig. 16, we compute unresolved circular polarization fractions for each of our models stepping through inclination from 5° to 175° in 5° increments. In addition to sampling different inclinations, we also make separate images for the times $7500~GM_{\bullet}~c^{-3}$ to $10~000~GM_{\bullet}~c^{-3}$, sampled in steps of $100~GM_{\bullet}~c^{-3}$. For a given model at a given inclination, the

filled region encloses the 5th to 95th percentiles of the range spanned by these models as a function of time, while the solid line marks the median. This reveals that constancy of the sign of *VII* over time occurs at some, but not all, inclinations for each model. In blue, we plot the results of normal radiative transfer (Normal RT), in orange we switch off Faraday rotation (No FR), and in green we switch off both Faraday rotation and intrinsic emission of circular polarization (No FR or Intrinsic).

The surprising amount of structure in the circular polarization curves as a function of inclination reflects the interplay of the three pathways to generate circular polarization. Even when facing the same side of the disc, it is possible to obtain both positive and negative circular polarization fractions. The 'Normal RT' curve is not perfectly antisymmetric about 90° because not all physical effects depend on inclination in the same way.

By comparing the blue 'Normal RT' curves with the orange 'No FR' curves, we see two regimes in which Faraday rotation affects the circularly polarized image. In the MAD model, which has mild values of τ_{ρ_V} , Faraday rotation shifts circular polarization fractions towards positive values for inclinations <90°, and towards negative values for inclinations >90°. This is because Faraday rotation is sensitive to the sign of the magnetic field, which is oriented vertically upwards in these models. In contrast, the SANE model is much more Faraday rotation thick, and hence Faraday rotation strongly suppresses the circular polarization, which in its absence could grow to values as large as 10 per cent. This is because, as shown in Fig. 10, the SANE model is much more Faraday conversion thick than the MAD model. Such a large circular polarization fraction is strongly ruled out by current constraints on M87* (≤0.8 per cent Kuo et al. 2014; Goddi et al. 2021). For some inclinations, this internal Faraday rotation can even change the sign of the unresolved circular polarization fraction. Finally, intrinsically emitted circular polarization modifies these curves in a similar direction by adding emission whose sign reflects the line-of-sight magnetic field direction, just like a small amount of Faraday rotation.

In summary, we find that the sign of the unresolved circular polarization fraction cannot easily be used to infer knowledge of the system without additional constraints. All three pathways to generate circular polarization are relevant and depend on inclination in different ways. Both models can exhibit constancy of the sign of the *VII* with time at some, but not all, inclinations.

5 DISCUSSION

536

5.1 Dipolar versus quadrupolar fields

The models considered in this work have dipolar magnetic fields, while a quadrupolar magnetic field is also possible (e.g. Beckwith, Hawley & Krolik 2008). A spun-up quadrupolar magnetic field would not exhibit a sign-flip in the tangential and radial components of the magnetic fields at the mid-plane. While the twist of these magnetic field structures would be qualitatively similar to that of a dipolar field, their field directions would not be. Hence, if the field were quadrupolar rather than dipolar, the intrinsic emission and Faraday rotation would be affected, but not the emission due to Faraday conversion. Since Faraday conversion dominates our images, we expect that circularly polarized images created with models with quadrupolar fields should be qualitatively similar to those created with dipolar fields.

5.2 Electron-positron plasmas

A substantial population of positrons may exist within these accretion flows via pair production (Begelman, Blandford & Rees 1984; Reynolds et al. 1996b; Wardle et al. 1998) that would modify the equations of polarized radiative transfer. As the ratio of positrons to electrons approaches unity, intrinsically emitted circular polarization and Faraday rotation vanish, while Faraday conversion doubles (Park & Blackman 2010; Enßlin, Hutschenreuter & Gopal-Krishna 2019; Anantua et al. 2020; Emami et al. 2021). Consequently, the existence of a positron population would result in images that would more directly encode the twist in the magnetic field geometry. In particular, the existence of positrons could strengthen the signature of magnetic twist in the photon ring described in Section 4.3.2.

5.3 Retrograde models

In a retrograde model, frame dragging operates in the opposite direction as the disc angular momentum that produces more complicated magnetic field geometries than sketched in Fig. 5. In Fig. 17, we plot the magnetic field decompositions of two retrograde models as in Fig. 6. In this plot, the z-axis remains aligned with both the vertical magnetic field direction and the disc angular momentum, but is now anti-aligned with the angular momentum of the SMBH. The magnetic field in the funnel region is twisted along with the SMBH angular momentum. In the MAD model, the field outside this region is twisted along with the disc, producing opposite twist orientations and directions of the toroidal field. Meanwhile, in the SANE model, we find that the azimuthal field direction only consistently follows the disc angular momentum in a thin shell around the funnel, beyond which the field becomes more turbulent, and in this model in alignment with the SMBH angular momentum again. We verify that this unexpected behaviour persists throughout times $t \in [7500, 10000]$ GM_{\bullet} c^{-3} . As a result, we expect that the imprint of this structure on circular polarization images would likely be more sensitive to the details of the plasma properties – where these transitions in magnetic field orientation occur, where the emission occurs, and where the Faraday effects occur.

Interestingly, the asymmetry of the image of M87* combined with its known jet orientation has constrained the motion of plasma on the sky as clockwise, and the orientation of the SMBH spin direction as away from us (see Event Horizon Telescope Collaboration 2019e for an extended discussion). If we can assume that the evacuated inner funnel region does not contribute much to the radiative transfer, then it is the angular momentum of the disc in the boundary region that matters when determining the twist, rather than that of the SMBH. Consequently, if M87*'s disc is prograde, we expect its photon ring to exhibit positive V, while if the disc is retrograde, we expect negative V instead. Future studies thoroughly exploring a wider variety of GRMHD and radiative transfer models would be useful in determining whether or not the sign of the circular polarization of the photon ring is a clean signature of prograde versus retrograde accretion.

5.4 Lower frequencies and larger spatial scales

Farther from the horizon, it is more straightforward to infer magnetic field properties free from the complications of event horizon scale magnetic field structure and light bending. If measurable, the combination of a rotation measure gradient across the jet, the pitch angle inferred from linear polarization ticks, and the sign of circular polarization can be used to determine the directions of both the toroidal and poloidal field components (Gabuzda 2018a; Gabuzda et al. 2008). Linear polarization maps exist for M87* at 43 GHz with sub-milliarcsecond resolution, and a full rotation measure analysis of this dataset is forthcoming (Walker et al. 2018). This information could help us associate regions of a resolved circularly polarized image in the millimetre to the photon ring and the different sides of the mid-plane.

5.5 Non-thermal electron distributions

This study was performed using only a single model of the electron distribution function (Mościbrodzka et al. 2016), distributed thermally. Meanwhile, the SEDs of these sources imply the existence of non-thermal electron populations to produce flux particularly in the near-infrared (Özel, Psaltis & Narayan 2000; Yuan, Quataert & Narayan 2003). Images including a non-thermal component to the electron distribution function in the form of a high-energy tail exhibit wider haloes of emission than purely thermal models (Özel et al. 2000; Mao, Dexter & Quataert 2017). Since we find that images of circular polarization on large scales are dominated by intrinsic emission, we hypothesize that the intrinsic emission signatures discussed in Section 4.2 may be strengthened. For faceon inclinations, this would preferentially add circular polarization with the line-of-sight sign of the magnetic field, while for edge-on inclinations, this would strengthen the 'four quadrants' pattern. We expect that additional Faraday effects would be weaker than the additional intrinsic emission, since Faraday rotation and conversion are inefficient for high-energy electrons. Light bending complications should also be weaker for a diffuse halo component. An additional non-thermal component at lower energies would increase Faraday effects, however. Overall, the effect of non-thermal electrons on circular polarization merits further study, and tractable prescriptions have been developed for the electron distribution function as a function of plasma β and magnetization σ that can be explored (Ball, Sironi & Ozel 2018; Davelaar et al. 2018, 2019).

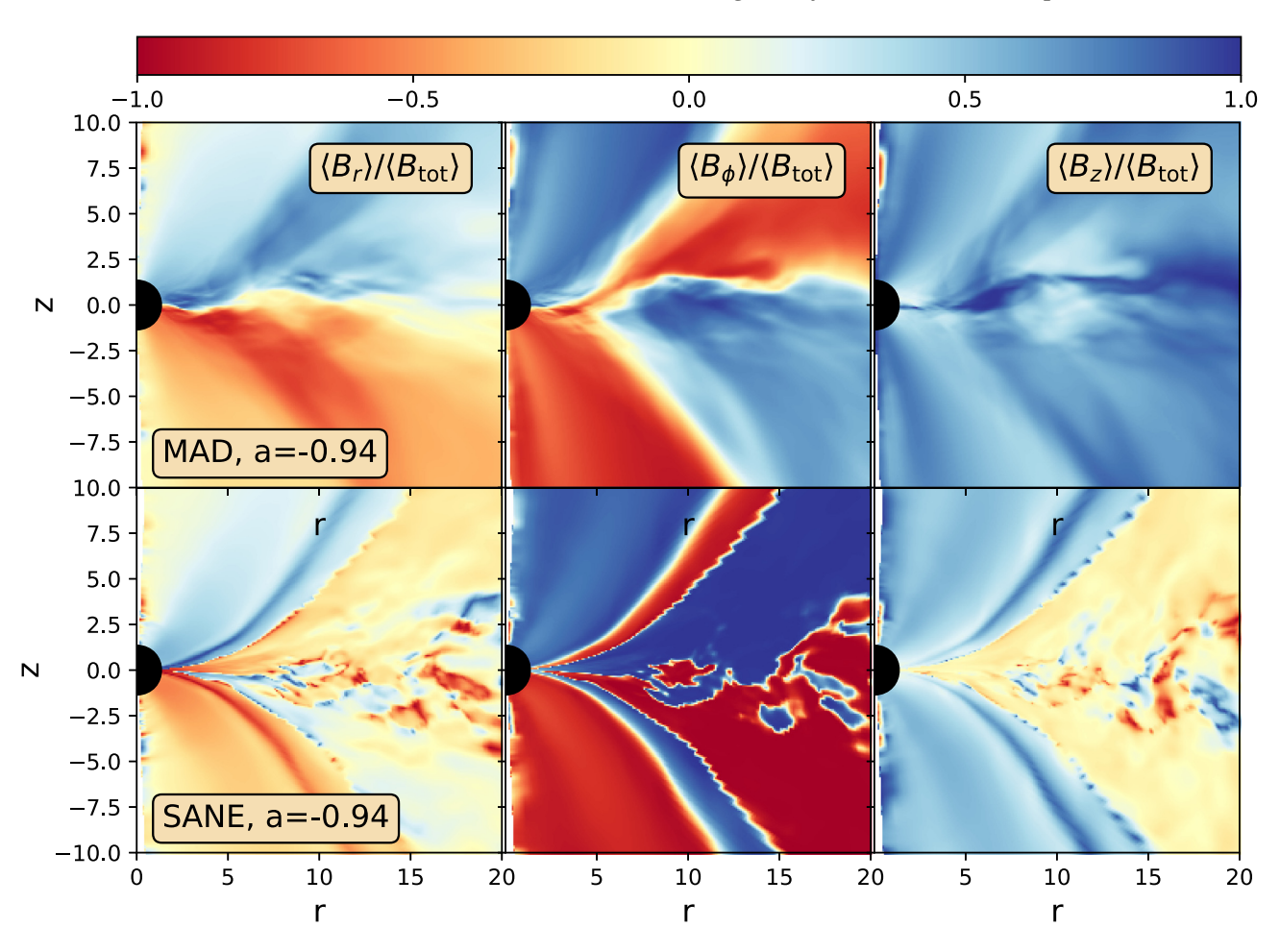


Figure 17. Magnetic field decompositions as in Fig. 6, but for retrograde models. In the funnel region, the magnetic field aligns with the SMBH. Beyond this region, in the MAD model, the field neatly switches azimuthal direction to align with the disc instead. However, in the SANE model, the field lines only align with the disc angular momentum in a narrow shell around the funnel. These additional features may produce more complicated circular polarization images depending on the details of how they are illuminated.

6 CONCLUSIONS

Using two GRMHD simulations of prograde accretion flows, we have studied the magnetic field structure and its imprint on circular polarization images. Our results are summarized as follows:

- (i) First, we explore the line of sight direction and twist of the magnetic field in these models that become imprinted on the circular polarization signal. The handedness of the magnetic twist flips across the mid-plane. In addition, we find that sign of the magnetic twist is different depending on whether the helix is viewed at edge-on versus pole-on viewing angles.
- (ii) Intrinsically emitted circular polarization carries the sign of the line-of-sight direction of the magnetic field. For edge-on viewing angles, this results in a 'four quadrants' pattern, also reported by Tsunetoe et al. (2020b). For face-on viewing angles, this mainly traces the vertical magnetic field direction, but is also sensitive to the radial component of the magnetic field behind the BH due to the lensing of photon orbits. Intrinsic emission produces relatively diffuse emission on large scales in these models.
- (iii) Circular polarization from Faraday conversion inherits the sign of Stokes U that we find is sensitive to the line-of-sight twist in the magnetic field. For edge-on viewing angles, we expect a sign flip across the mid-plane due to the switch in handedness of the magnetic twist. For pole-on viewing angles, we find that alternating

sub-images in the photon ring can flip sign. This is due to parallel transport and symmetries of the magnetic field.

- (iv) As discussed in previous works, a mild amount of Faraday rotation will imprint the line-of-sight direction of the magnetic field on the circular polarization (Tsunetoe et al. 2020a, b). However, too large an amount of Faraday rotation will scramble the circular polarization, even if the model is 'thin' to Faraday conversion. We notice the former in our MAD model, and the latter in our SANE model.
- (v) The circular polarization fraction and sign changes nontrivially with the inclination due to the complicated magnetic field geometry, different competing physical processes, and light bending. For a given model, it is possible to obtain either sign of circular polarization while viewing the same side of the disc.

This work represents an early step in decomposing and understanding circularly polarized images on event horizon scales. In future work, it will be useful to explore to what extent our findings generalize using different GRMHD and radiative transfer models. In particular, we plan on expanding our analysis to study the impact of non-thermal electron distributions and positron populations.

ACKNOWLEDGEMENTS

We thank Charles Gammie, George Wong, and Ben S Prather for support using their GRMHD simulations, IPOLE, and VISIT. We also thank Michael Johnson, Daniel Palumbo, Elizabeth Himwich, and Zachary Gelles for many fruitful and invigorating discussions about polarimetry, general relativity, and magnetic fields. Finally, we also thank our anonymous reviewers for their constructive comments which improved this work.

This material is based upon work supported by the National Science Foundation under Grant No. OISE 1743747. Computations at the Black Hole Initiative (BHI) were enabled by grants from the Gordon and Betty Moore Foundation and the John Templeton Foundation.

DATA AVAILABILITY

The data underlying this article will be shared on reasonable request to the corresponding author.

REFERENCES

Abramowicz M. A., Chen X., Kato S., Lasota J.-P., Regev O., 1995, ApJ, 438, L37

Aitken D. K., Greaves J., Chrysostomou A., Jenness T., Holland W., Hough J. H., Pierce-Price D., Richer J., 2000, ApJ, 534, L173

Anantua R., Emami R., Loeb A., Chael A., 2020, ApJ, 896, 30

Asada K., Nakamura M., 2012, ApJ, 745, L28

Ballantyne D. R., Özel F., Psaltis D., 2007, ApJ, 663, L17

Ball D., Sironi L., Özel F., 2018, ApJ, 862, 80

Beckert T., Falcke H., 2002, A&A, 388, 1106

Beckwith K., Hawley J. F., Krolik J. H., 2008, ApJ, 678, 1180

Begelman M. C., Blandford R. D., Rees M. J., 1984, Rev. Mod. Phys., 56, 255

Bisnovatyi-Kogan G. S., Lovelace R. V. E., Belinski V. A. (2002), ApJ, 580, 380

Bisnovatyi-Kogan G. S., Ruzmaikin A. A., 1974, Ap&SS, 28, 45

Bower G. C., Wright M. C. H., Falcke H., Backer D. C., 2003, ApJ, 588, 331

Bower G. C. et al., 2018, ApJ, 868, 101

Broderick A. E., Loeb A., 2006, MNRAS, 367, 905

Broderick A. E., McKinney J. C., 2010, ApJ, 725, 750

Bromley B. C., Melia F., Liu S., 2001, ApJ, 555, L83

Chael A., Narayan R., Johnson M. D., 2019, MNRAS, 486, 2873

Chatterjee K., Liska M., Tchekhovskoy A., Markoff S. B., 2019, MNRAS, 490, 2200

Childs H., et al., 2012, in High Performance Visualization–Enabling Extreme-Scale Scientific Insight, Chapman and Hall/CRC, New York, p. 357

Contopoulos I., Kazanas D., 1998, ApJ, 508, 859

Contopoulos I., Nathanail A., Sadowski A., Kazanas D., Narayan R. (2018), MNRAS, 473, 721

Davelaar J., Mościbrodzka M., Bronzwaer T., Falcke H., 2018, A&A, 612, A34

Davelaar J. et al., 2019, A&A, 632, A2

Dexter J., 2016, MNRAS, 462, 115

Emami R., Anantua R., Chael A. A., Loeb A., 2021, preprint (arXiv:2101.05327)

Enßlin T. A., 2003, A&A, 401, 499

Enßlin T. A., Hutschenreuter S., Gopal-Krishna, 2019, J. Cosmol. Astropart. Phys., 2019, 035

Event Horizon Telescope Collaboration, 2019a, ApJ, 875, L1

Event Horizon Telescope Collaboration, 2019b, ApJ, 875, L2

Event Horizon Telescope Collaboration, 2019c, ApJ, 875, L3

Event Horizon Telescope Collaboration, 2019d, ApJ, 875, L4

Event Horizon Telescope Collaboration, 2019e, ApJ, 875, L5

Event Horizon Telescope Collaboration, 2019f, ApJ, 875, L6

Event Horizon Telescope Collaboration, 2021a, ApJ, 910, L12

Event Horizon Telescope Collaboration, 2021b, ApJ, 910, L13

Gabuzda D., 2018a, Galaxies, 6, 9

Gabuzda D., 2018b, Galaxies, 7, 5

Gabuzda D. C., Vitrishchak V. M., Mahmud M., O'Sullivan S. P., 2008, MNRAS, 384, 1003

Gammie C. F., McKinney J. C., Tóth G., 2003, ApJ, 589, 444

Gebhardt K., Adams J., Richstone D., Lauer T. R., Faber S. M., Gültekin K., Murphy J., Tremaine S., 2011, ApJ, 729, 119

Goddi C. et al., 2021, ApJ, 910, L14

Himwich E., Johnson M. D., Lupsasca A. r., Strominger A., 2020, Phys. Rev. D, 101, 084020

Hodge P. E., 1982, ApJ, 263, 595

Ichimaru S., 1977, ApJ, 214, 840

Igumenshchev I. V., Narayan R., Abramowicz M. A., 2003, ApJ, 592,

Jiménez-Rosales A., Dexter J., 2018, MNRAS, 478, 1875

Johnson M. D. et al., 2020, Sci. Adv., 6, eaaz1310

Jones T. W., Odell S. L., 1977, ApJ, 214, 522

Kennett M., Melrose D., 1998, PASA, 15, 211

Kim J. Y. et al., 2019, A&A, 622, A196

Kormendy J., Ho L. C., 2013, ARA&A, 51, 511

Koutsantoniou L. E., Contopoulos I., 2014, ApJ, 794, 27

Koutsantoniou L. E., Contopoulos I., 2014, ApJ, 794, 27

Kuo C. Y. et al., 2014, ApJ, 783, L33

Mao S. A., Dexter J., Quataert E., 2017, MNRAS, 466, 4307

Marrone D. P., 2006, PhD thesis, Harvard University

Mościbrodzka M., Dexter J., Davelaar J., Falcke H., 2017, MNRAS, 468, 2214

Mościbrodzka M., Falcke H., Shiokawa H., 2016, A&A, 586, A38

Mościbrodzka M., Gammie C. F., 2018, MNRAS, 475, 43

Moscibrodzka M., Janiuk A., De Laurentis M., 2021, preprint (arXiv:2103.00267)

Muñoz D. J., Marrone D. P., Moran J. M., Rao R., 2012, ApJ, 745, 115

Narayan R., Igumenshchev I. V., Abramowicz M. A., 2003, PASJ, 55, L69

Narayan R., SÄ dowski A., Penna R. F., Kulkarni A. K., 2012, MNRAS, 426, 3241

Narayan R., Yi I., 1994, ApJ, 428, L13

Narayan R., Yi I., 1995, ApJ, 452, 710

Özel F., Psaltis D., Narayan R., 2000, ApJ, 541, 234

Palumbo D. C. M., Wong G. N., Prather B. S., 2020, ApJ, 894, 9

Pandya A., Zhang Z., Chandra M., Gammie C. F., 2016, ApJ, 822, 34

Park K., Blackman E. G., 2010, MNRAS, 403, 1993

Plambeck R. L. et al., 2014, ApJ, 797, 66

Porth O., Fendt C., Meliani Z., Vaidya B., 2011, ApJ, 737, 42

Rees M. J., Begelman M. C., Blandford R. D., Phinney E. S., 1982, Nature, 295, 17

Reynolds C. S., Di Matteo T., Fabian A. C., Hwang U., Canizares C. R., 1996a, MNRAS, 283, L111

Reynolds C. S., Fabian A. C., Celotti A., Rees M. J., 1996b, MNRAS, 283, 873

Ricarte A., Prather B. S., Wong G. N., Narayan R., Gammie C., Johnson M. D., 2020, MNRAS, 498, 5468

Ripperda B., Bacchini F., Philippov A. A., 2020, ApJ, 900, 100

Ruszkowski M., Begelman M. C., 2002, ApJ, 573, 485

Ryan B. R., Ressler S. M., Dolence J. C., Gammie C., Quataert E., 2018, ApJ, 864, 126

Sadowski A., Narayan R., Penna R., Zhu Y., 2013, MNRAS, 436, 3856

Semenov V., Dyadechkin S., Punsly B., 2004, Science, 305, 978

Shcherbakov R. V., Penna R. F., McKinney J. C., 2012, ApJ, 755, 133

Tsunetoe Y., Mineshige S., Ohsuga K., Kawashima T., Akiyama K., 2020a, PASJ, 72, 32

Tsunetoe Y., Mineshige S., Ohsuga K., Kawashima T., Akiyama K., 2020b, preprint (arXiv:2012.05243)

Walker R. C., Hardee P. E., Davies F. B., Ly C., Junor W., 2018, ApJ, 855, 128

Wardle J. F. C., Homan D. C., 2001, in Laing R. A., Blundell K. M., eds, ASP Conf. Ser. Vol. 250, Particles and Fields in Radio Galaxies Conference, Astron. Soc. Pac., San Francisco, p. 152

Wardle J. F. C., Homan D. C., 2003, Ap&SS, 288, 143

Wardle J. F. C., Homan D. C., Ojha R., Roberts D. H., 1998, Nature, 395, 457

Yuan F., Narayan R., 2014, ARA&A, 52, 529

Yuan F., Quataert E., Narayan R., 2003, ApJ, 598, 301

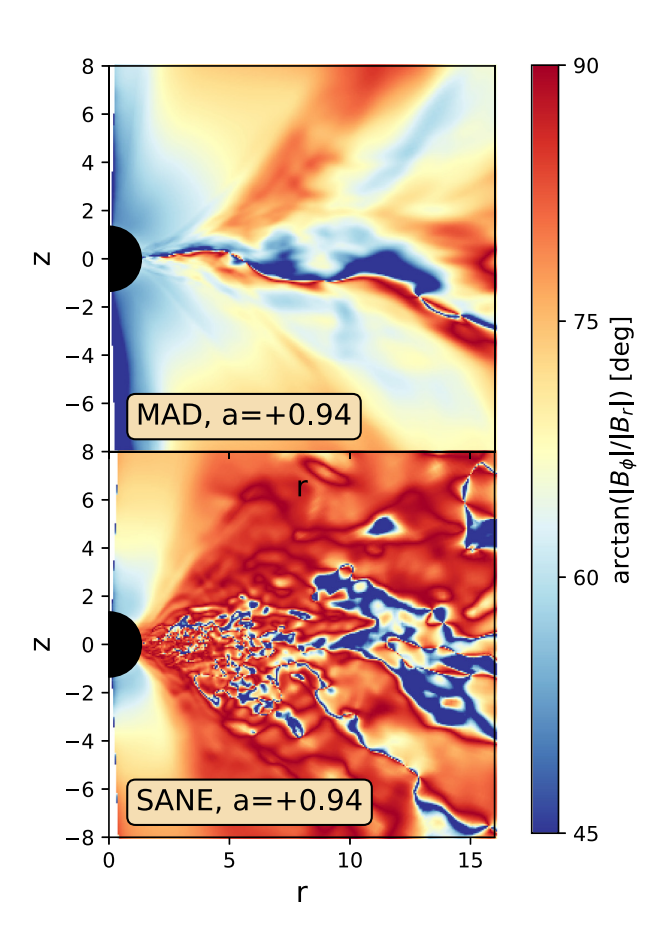


Figure A1. By examining the angle of the magnetic field projected on to the xy-plane, we can affirm the sense of vertical twist illustrated in Fig. 5. Here, an angle of 45° implies that $|B_\phi| = |B_r|$, while an angle of 90° implies that $|B_\phi| \gg |B_r|$. At least in the funnel region, this angle increases as |z| increases. This is not true in the disc of the turbulent SANE, where indeed our time-averaged V image reveals weak edge-on polarization.

APPENDIX A: CONFIRMING VERTICAL TWIST IN OUR GRMHD MODELS

In Fig. A1, we confirm the sense of 'vertical twist' sketched in Fig. 5. Ignoring the vertical component, we plot the angle made by the magnetic field in the xy plane, $\arctan |B_{\phi}|/|B_r|$. An angle of 45° implies that the radial and azimuthal fields are equal in magnitude, while an angle of 90° implies that the toroidal field is much stronger. At fixed r, this angle increases as one moves away from the midplane, resulting in the vertical twist shown in Fig. 5. However, this is only clear in the funnel region of the SANE model, outside of which the field remains consistently toroidally dominated and turbulent. The vertical twist can also be inferred by close inspection of the pole-on viewing angles in Fig. 7. The red curves that are anchored around the BH, which tend to extend to larger |z|, sweep more circular arcs than the blue curves anchored in the disc.

APPENDIX B: EMISSIVITY AND ROTATIVITY IN REPRESENTATIVE PIXELS

In Fig. B1, we examine representative pixels in each of the models during their final snapshot, marked with white circles in Fig. 10. Along each of these lines of sight, we plot frame-invariant emissivities (j/v^2 ; upper panels) and rotativities ($v\rho$; lower panels) as a function of radius in Kerr–Schild coordinates, r_{KS} (see Mościbrodzka & Gammie 2018 for more details). In the rotativity panels, we omit

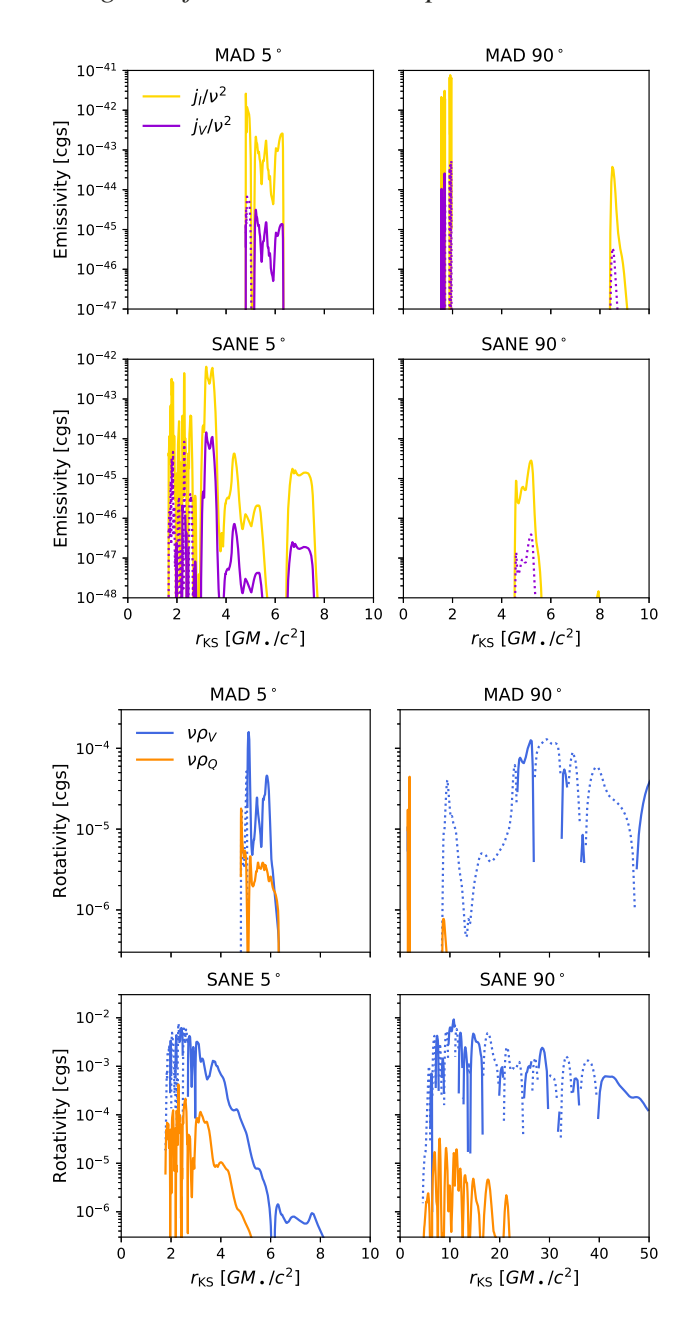


Figure B1. Frame-invariant emissivities (upper panels) and rotativities (lower panels) for representative lines of sight marked with white circles in Fig. 10. We find that both emission and Faraday conversion are enclosed well within the outer integration radius of $20~GM_{\bullet}~c^{-2}$, although Faraday rotation continues out to large radius at 90° inclinations.

sections of the geodesic where less than 1 per cent of the final emission along the line of sight has been produced. This allows us to ignore Faraday rotation and conversion in areas behind the bulk of the emission that do not affect the observables. This analysis reveals that both the emission and Faraday conversion are enclosed within the outer integration radius of $20~GM_{\bullet}~c^{-2}$ chosen for the radiative transfer. For 90° inclinations, Faraday rotation continues to large radius, as also shown in Ricarte et al. (2020), but this does not affect the circular polarization.

This paper has been typeset from a TEX/IATEX file prepared by the author.